

# Catastrophic Evaporation of Rocky Planets

Daniel Perez-Becker<sup>1</sup><sup>★</sup> and Eugene Chiang<sup>2</sup>

<sup>1</sup>*Department of Physics, University of California at Berkeley, 366 LeConte Hall, Berkeley CA 94720-7300, USA*

<sup>2</sup>*Departments of Astronomy and of Earth and Planetary Science, University of California at Berkeley, Hearst Field Annex B-20, Berkeley CA 94720-3411, USA*

Submitted: 14 August 2018

## ABSTRACT

Short-period exoplanets can have dayside surface temperatures surpassing 2000 K, hot enough to vaporize rock and drive a thermal wind. Small enough planets evaporate completely. We construct a radiative-hydrodynamic model of atmospheric escape from strongly irradiated, low-mass rocky planets, accounting for dust-gas energy exchange in the wind. Rocky planets with masses  $\lesssim 0.1 M_{\oplus}$  (less than twice the mass of Mercury) and surface temperatures  $\gtrsim 2000$  K are found to disintegrate entirely in  $\lesssim 10$  Gyr. When our model is applied to Kepler planet candidate KIC 12557548b — which is believed to be a rocky body evaporating at a rate of  $\dot{M} \gtrsim 0.1 M_{\oplus}/\text{Gyr}$  — our model yields a present-day planet mass of  $\lesssim 0.02 M_{\oplus}$  or less than about twice the mass of the Moon. Mass loss rates depend so strongly on planet mass that bodies can reside on close-in orbits for Gyrs with initial masses comparable to or less than that of Mercury, before entering a final short-lived phase of catastrophic mass loss (which KIC 12557548b has entered). Because this catastrophic stage lasts only up to a few percent of the planet’s life, we estimate that for every object like KIC 12557548b, there should be 10–100 close-in quiescent progenitors with sub-day periods whose hard-surface transits may be detectable by *Kepler* — if the progenitors are as large as their maximal, Mercury-like sizes (alternatively, the progenitors could be smaller and more numerous). According to our calculations, KIC 12557548b may have lost  $\sim 70\%$  of its formation mass; today we may be observing its naked iron core.

## Key words:

hydrodynamics – planets and satellites: atmospheres – planets and satellites: composition – planets and satellites: physical evolution – planet-star interaction

## 1 INTRODUCTION

Atmospheric escape shapes the faces of planets. Mechanisms for mass loss vary across the Solar System. Planets lacking magnetic fields can be stripped of their atmospheres by the Solar wind: the atmospheres of both Mercury and Mars are continuously eroded and refreshed by Solar wind ions (Potter & Morgan 1990, 1997; Lammer & Bauer 1997; Bida et al. 2000; Killen et al. 2004; Jakosky & Phillips 2001). Venus demonstrates the extreme sensitivity of atmospheres to stellar insolation. Although its distance to the Sun is only 30% less than that of the Earth, Venus has lost its water to hydrodynamic escape powered by Solar radiation (Kasting & Pollack 1983; Zahnle & Kasting 1986). Impacts with comets and asteroids can also purge planets of their atmospheres, as has thought to have happened to some extent on Mars (Melosh & Vickery 1989; Jakosky & Phillips 2001) and

some giant planet satellites (Zahnle et al. 1992). An introductory overview of atmospheric escape in the Solar System is given by Catling & Zahnle (2009).

Smaller bodies lose their atmospheres more readily because of their lower surface gravities. Bodies closer to their host star also lose more mass because they are heated more strongly. Extrasolar planets on close-in orbits are expected to have highly processed atmospheres. In extreme cases, stellar irradiation might even evaporate planets in their entirety — comets certainly fall in this category.

Hot Jupiters are the best studied case for atmospheric erosion in extrasolar planets (for theoretical models, see Yelle 2004, 2006; Tian et al. 2005; García Muñoz 2007; Holmström et al. 2008; Murray-Clay et al. 2009; Ekenbäck et al. 2010; Tremblin & Chiang 2013). For these gas giants, mass loss is driven by stellar ultraviolet (UV) radiation which photo-ionizes hydrogen and imparts enough energy per proton to overcome the planet’s large escape velocity ( $\sim 60$  km/s). Mass loss for hot Jupiters typically occurs at a rate of  $\dot{M} \sim 10^{10}–10^{11}$  g/s

<sup>★</sup> e-mail: perez-becker@berkeley.edu

so that  $\sim 1\%$  of the planet mass is lost over its lifetime (Yelle 2006; García Muñoz 2007; Murray-Clay et al. 2009). Although this erosion hardly affects a hot Jupiter’s internal structure, the outflow is observable. Winds escaping from hot Jupiters have been spectroscopically detected by the *Hubble Space Telescope* (HST). During hot Jupiter transits, several absorption lines (H I, O I, C II, Mg II, and Si III) deepen by  $\sim 2\text{--}10\%$  (Vidal-Madjar et al. 2003, 2004, 2008; Ben-Jaffel 2007, 2008; Fossati et al. 2010; Lecavelier Des Etangs et al. 2010; Linsky et al. 2010; Lecavelier des Etangs et al. 2012).

Because of their lower escape velocities, lower mass super-Earths should have their atmospheres more significantly sculpted by evaporation. Lopez et al. (2012) found that hydrogen-dominated atmospheres of close-in super-Earths could be stripped entirely by UV photoevaporation (e.g., Kepler-11b).

At even lower masses and stellocentric distances, planets might evaporate altogether. When dayside temperatures surpass  $\sim 2000$  K, rocks, particularly silicates and iron (and to a lesser extent, Ti, Al, and Ca), begin to vaporize. If the planet mass is low enough, thermal velocities of the high-metallicity vapor could exceed escape velocities. Under these circumstances, mass loss is not limited by stellar UV photons, but is powered by the incident bolometric flux.

### 1.1 KIC 12557548b: A Catastrophically Evaporating Planet

In fact, the *Kepler* spacecraft may have enabled the discovery of an evaporating, close-in rocky planet near the end of its life. As reported by Rappaport et al. (2012), the K-star KIC 12557548 dims every 15.7 hours by a fractional amount  $f$  that varies erratically from a maximum of  $f \approx 1.3\%$  to a minimum of  $f \lesssim 0.2\%$ . These occultations are thought to arise from dust embedded in the time-variable outflow emitted by an evaporating rocky planet — hereafter KIC 1255b. Because *Kepler* observes in the broadband optical, the obscuring material cannot be gas which absorbs only in narrow lines; it must take the form of dust which absorbs and scatters efficiently in the continuum. As we will estimate shortly, the amount of dust lost by the planet is prodigious.

From the  $\sim 2000$  K surface of the planet is launched a thermal (“Parker-type”) wind out of which dust condenses as the gas expands and cools. The composition of the high-metallicity wind reflects the composition of the evaporating rocky planet (see, e.g., Schaefer & Fegley 2009): the wind may consist of Mg, SiO, O, and O<sub>2</sub> — and Fe if it has evaporated down to its iron core. Stellar gravity, together with Coriolis and radiation-pressure forces, then shape the dusty outflow into a comet-like tail. The peculiar shape of the transit light curve of KIC 1255b supports the interpretation that the occultations are caused by a dusty tail. First, the light curve evinces a flux excess just before ingress, which could be caused by the forward scattering of starlight toward the observer. Second, the flux changes more gradually during egress than during ingress, as expected for a trailing tail. Both features of the light curve and their explanations were elucidated by Rappaport et al. (2012), and further quantified by Brogi et al. (2012) who presented a phenomenological light-scattering model of a dusty tail.<sup>1</sup>

<sup>1</sup> Alternative ideas might include Roche lobe overflow from a companion to the star (c.f. Lai et al. 2010). A problem with this scenario is that the mass transfer accretion stream, funneled through the L1 Lagrange point,

Spectra of KIC 12557548 taken using the Keck Telescope reveal no radial velocity variations down to a limiting accuracy of  $\sim 100$  m/s (A. Howard and G. Marcy 2012, personal communication). A deep Keck image also does not reveal any background blended stars. These null results are consistent with the interpretation that KIC 1255b is a small, catastrophically evaporating planet.

The characteristic mass loss rate for KIC 1255b — a quantity that we will reference throughout this paper — can be estimated from the observations as follows. First compute the total mass in grains required to absorb/scatter a fraction  $f$  of the starlight, assuming that the dust is optically thin (or marginally so). Out of the total area  $\pi R_*^2$  presented by the stellar face, take the dust cloud to cover an area  $A$  and to have a characteristic line-of-sight optical depth  $\Sigma_d \kappa_d$ , where  $\Sigma_d$  is the grain mass per unit area (on the sky) and  $\kappa_d$  is the grain opacity. Then

$$f = \frac{A}{\pi R_*^2} \Sigma_d \kappa_d. \quad (1)$$

Assume further that grains can be modeled as a monodispersion of spheres with radii  $s$  and internal material density  $\rho_{\text{int}}$  so that

$$\kappa_d = \frac{3}{4\rho_{\text{int}} s}. \quad (2)$$

The total mass in dust covering the star is then

$$M_d = \Sigma_d A = \frac{4\pi}{3} f \rho_{\text{int}} R_*^2 s. \quad (3)$$

To obtain a mass loss rate, divide this mass by the orbital period of 15.7 hours on the grounds that transit depths change by up to an order of magnitude from orbit to orbit. For  $f = 1\%$  — when KIC 1255b is in a state of relatively high mass loss — the resultant mass loss rate in grains is

$$\dot{M}_{1255b, \text{dust}} \sim 0.4 \left( \frac{R_*}{0.65 R_\odot} \right)^2 \left( \frac{f}{0.01} \right) \left( \frac{s}{0.5 \mu\text{m}} \right) \left( \frac{\rho_{\text{int}}}{1 \text{ g/cm}^3} \right) M_\oplus \text{Gyr}^{-1}. \quad (4)$$

This is the mass loss rate in dust only, by construction. The gas-to-dust ratio by mass,  $\eta$ , must be at least on the order of unity if outflowing gas is to carry, by Epstein drag, embedded grains out of the gravity well of the planet (Rappaport et al. 2012). Henceforth we will adopt as our fiducial total mass loss rate (for the relatively high value of  $f = 1\%$ ):

$$\dot{M}_{1255b} = (1 + \eta) \dot{M}_{1255b, \text{dust}} \sim 1 M_\oplus \text{Gyr}^{-1}. \quad (5)$$

would lead the companion in its orbit, not trail it as is required by observation. By comparison, in our dusty wind model, there is no focussing of material at L1 because the wind is not in hydrostatic equilibrium and therefore does not conform to Roche lobe equipotentials. Moreover, stellar radiation pressure, usually neglected in standard Roche-overflow models, is crucial for diverting the flow so that it trails the planet in its orbit (see also Mura et al. 2011). Another alternative involves bow shocks of planets passing through stellar coronae (Vidotto et al. 2010, 2011a,b; Llama et al. 2011; Tremblin & Chiang 2013) which may explain the ingress-egress asymmetry observed for the exoplanet WASP-12b (Fossati et al. 2010). Bow shocks between the planetary wind and the stellar wind are also expected to occur for KIC 1255b, but would be hard to detect through *Kepler*’s broadband filter since the shocked gas alone would absorb only in narrow absorption lines. At the low gas densities characterizing exoplanet winds, only dust can generate the large continuum opacities required by the deep transits observed by *Kepler*. Rappaport et al. (2012) reviews these and additional arguments supporting the dust tail model. A similar interpretation was proposed for the light curve of beta Pictoris (Lecavelier Des Etangs et al. 1997; Lamers et al. 1997).

The total mass loss rate  $\propto \rho_{\text{int}} s (1 + \eta)$ . Given the uncertainties in these three factors (some rough guesses:  $\rho_{\text{int}} \gtrsim 0.5 \text{ g cm}^{-3}$  for possibly porous grains;  $s \gtrsim 0.1 \mu\text{m}$ ;  $\eta \gtrsim 1$ ), the total mass loss rate could take any value  $\dot{M}_{1255b} > 0.1 M_{\oplus} / \text{Gyr}$  (but see also our Figures 8 and 10 which place upper bounds on mass loss rates).

Rappaport et al. (2012) claimed that the present-day mass of KIC 1255b is  $\sim 0.1 M_{\oplus}$ . They estimated, to order-of-magnitude, the maximum planet mass that could reproduce the observed mass loss rate given by equation (5). Here we revisit the issue of planet mass — and the evaporative lifetime it implies — with a first-principles solution of the hydrodynamic equations for a planetary wind, including an explicit treatment of dust-gas thermodynamics. We will obtain not only improved estimates of the present-day mass, but also full dynamical histories of KIC 1255b.

## 1.2 Plan of This Paper

We develop a radiative-hydrodynamic wind model to study mass loss of close-in rocky planets with dayside temperatures high enough to vaporize rock. Although our central application will be to understand KIC 1255b — both today and in the past — the model is general and can be easily be modified for parameters of other rocky planets.

The paper is structured as follows. In §2 we present the model that computes  $\dot{M}$  as a function of planet mass  $M$ . We give results in §3, including estimates for the maximum present-day mass and the maximum formation mass of KIC 1255b. A wide-ranging discussion of the implications of our results — including, e.g., an explanation of why mass loss in this context does not obey the often-used energy-limited mass loss formula (cf. Lopez et al. 2012), as well as the prospects of detecting close-in Mercuries and stripped iron cores — is given in §4. Our findings are summarized in §5.

## 2 THE MODEL

We construct a 1D model for the thermally-driven atmospheric mass loss from a close-in rocky planet, assuming that it occurs in the form of a transonic Parker wind. The atmosphere of the planet consists of a high-metallicity gas created by the sublimation of silicates (and possibly iron, as we discuss in §4.7) from the planetary surface. We focus on the flow that streams radially toward the star from the substellar point on the planet. The substellar ray is of special interest because the mass flux it carries will be maximal insofar as the substellar point has the highest temperature — and thus the highest rate of rock sublimation — and insofar as stellar gravity will act most strongly to accelerate gas away from the planet.

As the high-metallicity gas flows away from the surface of the planet, it will expand and cool, triggering the condensation of dust grains. Dust grains can affect the outflow in several ways: (a) latent heat released during the condensation of grains will heat the gas; (b) continuously heated by starlight, grains will transfer their energy to the gas via gas-grain collisions; and (c) absorption/scattering of starlight by grains will reduce the stellar flux reaching the planet, reducing the surface temperature and sublimation rate. In this work, we do not account for the microphysics of grain condensation, as cloud formation is difficult to calculate from first principles (see, e.g., the series of five papers beginning with Helling et al. 2001; see also Helling et al. 2008a and Helling et al. 2008b). Instead, we treat the dust-to-gas mass fraction  $x_{\text{dust}}$  as a free function and explore

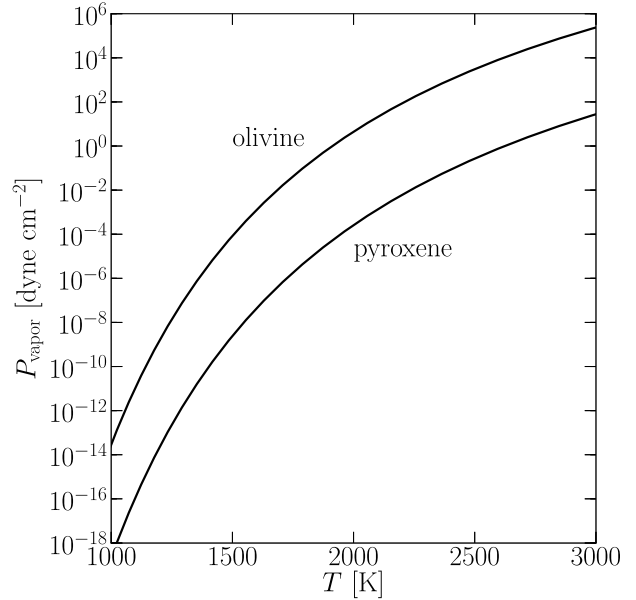


**Figure 1.** Equilibrium vapor pressures of pyroxene and olivine vs. temperature, obtained from equation (7).

how our results depend on this function. In our 1-fluid model, dust grains are perfectly entrained in the gas flow, an assumption we test *a posteriori* (§4.2).

We begin in §2.1 by evaluating thermodynamic variables at the surface of the planet — the inner boundary of our model. In §2.2 we introduce the 1D equations of mass, momentum, and energy conservation. In §2.3 we explain the relaxation method employed to solve the conservation laws.

### 2.1 Base Conditions of the Atmosphere

Dayside planet temperatures peak at approximately

$$T_{\text{surface}} \approx T_* \sqrt{\frac{R_*}{a}} e^{-\tau_{\text{surface}}/4} \approx 2150 e^{-\tau_{\text{surface}}/4} \text{ K}, \quad (6)$$

where for our numerical evaluation we have used parameters appropriate to KIC 12557548 (orbital semimajor axis  $a \approx 0.013 \text{ AU}$ ; effective stellar temperature  $T_* \approx 4450 \text{ K}$ ; and stellar radius  $R_* \approx 0.65 R_{\odot}$ ; Rappaport et al. 2012). Here  $\tau_{\text{surface}}$  is the optical depth between the planet’s surface and the star due to absorption/scattering by dust grains.

We expect rocky extrasolar planets to consist of the same silicates predominantly found in the mantle of the Earth: pyroxene ( $[\text{Fe,Mg}] \text{SiO}_3$ ) and olivine ( $[\text{Fe,Mg}]_2 \text{SiO}_4$ ). At the estimated  $T_{\text{surface}}$ , these silicates will vaporize and form an atmosphere whose equilibrium vapor pressure can be described by

$$P_{\text{vapor}} = \exp \left( -\frac{m L_{\text{sub}}}{k T_{\text{surface}}} + b \right), \quad (7)$$

where  $m$  is the mass of either a pyroxene or olivine molecule,  $k$  is Boltzmann’s constant,  $L_{\text{sub}}$  is the latent heat of sublimation, and  $b$  is a constant. We follow Kimura et al. (2002) in our choice of parameters for equation (7). For olivine,  $m = 169 m_{\text{H}}$  ( $\text{Mg}_{1.1} \text{Fe}_{0.9} \text{SiO}_4$ ) where  $m_{\text{H}}$  is the mass of atomic hydrogen,  $L_{\text{sub}} = 3.21 \times 10^{10}$

erg g<sup>-1</sup>, and  $e^b = 6.72 \times 10^{14}$  dyne cm<sup>-2</sup>; these values were found experimentally by evaporating forsterite (Mg<sub>2</sub>SiO<sub>4</sub>), an end-member of olivine (Nagahara et al. 1994). For pyroxene,  $m = 60$  m<sub>H</sub>,  $L_{\text{sub}} = 9.61 \times 10^{10}$  erg g<sup>-1</sup>, and  $e^b = 3.13 \times 10^{11}$  dyne cm<sup>-2</sup>; these values were determined by Hashimoto (1990) for SiO<sub>2</sub>. Kimura et al. (2002) argue that the parameters for SiO<sub>2</sub> are appropriate for pyroxene because evaporation experiments of enstatite (MgSiO<sub>3</sub>) show that SiO<sub>2</sub> escapes preferentially, leaving the mineral with a polycrystalline forsterite coating (Tachibana et al. 2002). We plot equation (7) for both olivine and pyroxene in Figure 1.

According to Schaefer & Fegley (2009), the atmosphere of a hot rocky planet at temperatures similar to  $T_{\text{surface}}$  is primarily composed of Mg, SiO, O, and O<sub>2</sub>. In our model we choose a mean molecular weight for the atmospheric gas of

$$\mu = 30 \text{ m}_H, \quad (8)$$

similar to the average molecular mass of Mg and SiO. Additionally, we set the adiabatic index of the gas to be  $\gamma \equiv c_p/c_v = 1.3$ , appropriate for diatomic gases at high temperatures (e.g.,  $\gamma_{\text{H}_2}^{T=2000\text{K}} = 1.318$ , Lange & Forker 1967). The gas density at the surface of the planet is

$$\rho_{\text{vapor}} = \frac{\mu P_{\text{vapor}}}{k T_{\text{surface}}}. \quad (9)$$

## 2.2 Equations Solved

In our 1D hydrodynamic model, we solve the equations for mass, momentum, and energy conservation of the gas, assuming a steady flow. From mass conservation,

$$\frac{\partial}{\partial r}(r^2 \rho v) = 0, \quad (10)$$

where  $r$  is the radial distance from the center of the planet, and  $\rho$  and  $v$  are the density and velocity of the gas. In the frame rotating at the orbital angular frequency of the planet, momentum conservation — with the Coriolis force omitted — implies

$$\rho v \frac{\partial v}{\partial r} = -\frac{\partial P}{\partial r} - \frac{GM\rho}{r^2} + \frac{3GM_*\rho r}{a^3}, \quad (11)$$

where  $G$  is the gravitational constant,  $P = \rho kT/\mu$  is the gas pressure,  $T$  is the gas temperature, and  $M$  and  $M_* = 0.7M_{\odot}$  are the masses of the planet and the host star (KIC 12557548), respectively. The last term on the right-hand side of eq. (11), which we refer to as the tidal gravity term, is the sum of the centrifugal force and the gravitational attraction from the star. In deriving eq. (11), we have neglected terms of order  $(r/a)^2$ . We do not include the contribution of the Coriolis force because its magnitude will only be comparable to the gravitational attraction of the planet when the gas moves at bulk speeds comparable to the escape velocity of the planet at its Hill sphere (a.k.a. the Roche lobe). This generally occurs near the outer boundary of our calculation, which is set by the location of the sonic point. Although the sonic point radius and Hill sphere radius are distinct quantities, we will find in practice for our models that they are close to one another, which is not surprising since the wind most easily accelerates to supersonic velocities where the effective gravity is weakest — i.e., near the Hill sphere.

The steady-state energy conservation equation,  $\nabla \cdot (\rho u \mathbf{v}) = -P \nabla \cdot \mathbf{v} + \Gamma$ , together with equation (10) and the specific internal energy  $u = kT/[(\gamma - 1)\mu]$ , yields

$$\rho v \frac{\partial}{\partial r} \left[ \frac{kT}{(\gamma - 1)\mu} \right] = \frac{kT v}{\mu} \frac{\partial \rho}{\partial r} + \Gamma_{\text{col}} + \Gamma_{\text{lat}}. \quad (12)$$

The left hand side of equation (12) tracks changes in internal energy, while the terms on the right hand side track cooling due to  $PdV$  work, heating from gas-grain collisions, and latent heat released from grain condensation. We have omitted conduction because we found it to be negligible compared to all other terms.

For gas heating by dust-gas collisions, we assume that each collision between a gas molecule and a dust grain transfers an energy  $k(T_{\text{dust}} - T)$  to the gas molecule. Then the rate of gas heating per unit volume is

$$\Gamma_{\text{col}} = \frac{3x_{\text{dust}}}{4s\rho_{\text{int}}} \frac{k}{\mu} (T_{\text{dust}} - T) \rho^2 c_s, \quad (13)$$

where  $x_{\text{dust}}(r) \equiv \rho_{\text{dust}}/\rho$  is the spatially varying dust-to-gas mass ratio,  $s = 1 \mu\text{m}$  is the assumed grain size,  $\rho_{\text{int}} = 3 \text{ g cm}^{-3}$  is the grain bulk density, and

$$c_s = \sqrt{\frac{\gamma k T}{\mu}} \quad (14)$$

is the sound speed of the gas. As discussed in §4.2, our assumption that micron-sized grains are entrained in the flow is valid for the lowest mass planets we consider (a group that includes, as best we will gauge, KIC 1255b) but not the highest mass planets.

We adopt

$$T_{\text{dust}} = T_* \sqrt{\frac{R_*}{a}} e^{-\tau/4} \quad (15)$$

for simplicity, so that  $T_{\text{dust}}$  equals  $T_{\text{surface}}$  at the surface of the planet. The dust optical depth to starlight from  $r$  to the star is

$$\tau = \frac{3}{4s\rho_{\text{int}}} \int_r^{r_s} \rho x_{\text{dust}} dr + \tau_s. \quad (16)$$

The constant  $\tau_s$  accounts for the optical depth from the outer boundary of our calculation — the sonic point radius  $r_s$  — to the star. We arbitrarily set

$$\tau_s = 0.01. \quad (17)$$

Our results are insensitive to our assumed value of  $\tau_s$  as long as it is  $\ll 1$ . The optical depth at the planet's surface is  $\tau_{\text{surface}} \equiv \tau(r = R)$ , where  $R$  is the planetary radius, calculated for a given  $M$  by assuming a constant bulk density of  $5.4 \text{ g/cm}^3$ , the mean density of Mercury.

Latent heat from grain formation is released at a rate given by

$$\Gamma_{\text{lat}} = L_{\text{sub}} \rho v \frac{dx_{\text{dust}}}{dr}, \quad (18)$$

where we have used  $L_{\text{sub}}$  appropriate for pyroxene, as it is more thermally stable than olivine (see Figure 1; in any case,  $L_{\text{sub}}$  for olivine is not that different).

Because we do not model dust condensation from first principles, the dust-to-gas mass ratio  $x_{\text{dust}}(r)$  is a free function, which we parametrize as follows:

$$\log[x_{\text{dust}}(r)] = \log(x_{\text{dust,max}}) - \log(x_{\text{dust,amp}}) \cdot \left\{ 1 - \arctan \left[ \frac{8(r - R)}{3(r_s - R)} \right] \left[ \arctan \left( \frac{8}{3} \right) \right]^{-1} \right\}. \quad (19)$$

The function  $x_{\text{dust}}$  increases monotonically with  $r$  to a maximum value of  $x_{\text{dust,max}}$ , starting from a minimum value of



$x_{\text{dust, max}}/x_{\text{dust, amp}}$ . We have two reasons for choosing  $x_{\text{dust}}$  to increase rather than decrease with increasing height. The first is physical: as the wind launches into space, it expands and cools, allowing the metal-rich vapor to more easily saturate and condense (see also §4.8). The second is motivated by observations: on length scales on the order of the stellar radius, far from the planet, the wind must have a relatively high dust content so as to produce the deep transits observed by *Kepler*. Of course, neither of these reasons constitutes a first-principles proof that  $x_{\text{dust}}$  actually does increase with  $r$ . Indeed the increasingly low density of the wind may frustrate condensation. A physics-based calculation of how grains may (or may not) form in the wind is sorely needed (§4.8); our present study merely parameterizes this difficult problem.

As dust condenses from gas and  $x_{\text{dust}}$  rises, the gas density  $\rho$  must fall by mass conservation. For simplicity we neglect the dependence of  $\rho$  on  $x_{\text{dust}}$  and so restrict our analysis to  $x_{\text{dust, max}} \ll 1$ ; in practice, the maximum value of  $x_{\text{dust, max}}$  that we consider is  $10^{-0.5} \approx 0.32$ .

### 2.3 Relaxation Code

The structure of the wind is found by the simultaneous solution of equations (10), (11), (12), & (16) with the appropriate boundary conditions. This system constitutes a two-point boundary value problem, as the boundary conditions for  $\rho$  and  $T$  are defined at the base of the flow, while those for  $v$  and  $\tau$  are defined at the sonic point.

Although generally more complicated, relaxation codes are preferred over shooting methods when solving for the transonic Parker wind. This is because for each transonic solution there are an infinite number of “breeze solutions” where the bulk speed of the wind never reaches supersonic velocities. It is easier to begin with an approximate solution that already crosses the sonic point and to then refine this solution, than to exhaustively shoot in multidimensional space for the sonic point. Murray-Clay et al. (2009) used a relaxation code to find the transonic wind from a hot Jupiter. Here we follow their methodology; we develop a relaxation code based on Section 17.3 of Press et al. (1992).

#### 2.3.1 Finite Difference Equations

We set up a grid of  $N = 100$  logarithmically spaced radii that run from the base of the flow located at the surface of the planet ( $r = R$ ) to the sonic point ( $r = r_s$ ). We replace our system of differential equations by a set of finite-difference relations. For  $\rho$  and  $T$ :

$$\begin{aligned} E_{1,j} &\equiv \Delta_j \rho - \frac{d\rho}{dr} \Delta_j r \\ &= \Delta_j \rho + \rho \left( \frac{2}{r} + \frac{1}{v} \frac{dv}{dr} \right) \Delta_j r = 0, \end{aligned} \quad (20)$$

$$\begin{aligned} E_{2,j} &\equiv \Delta_j T - \frac{dT}{dr} \Delta_j r \\ &= \Delta_j T - (\gamma - 1) \left[ \frac{T}{\rho} \frac{d\rho}{dr} + \frac{\mu}{k\rho v} (\Gamma_{\text{col}} + \Gamma_{\text{lat}}) \right] \Delta_j r = 0, \end{aligned} \quad (21)$$

where finite differences are calculated upwind ( $\Delta_j x \equiv x_j - x_{j-1}$ ), as  $\rho$  and  $T$  (and by extension  $E_1$  and  $E_2$ ) have boundary conditions defined at the surface of the planet ( $j = 0$ ). Following Press et al. (1992), we average across adjacent grid points when

evaluating variables in (20) and (21), e.g.,  $\rho \equiv (\rho_{j-1} + \rho_j)/2$ . The finite-difference relations for  $v$  and  $\tau$  are:

$$\begin{aligned} E_{3,j} &\equiv \Delta_j v - \frac{dv}{dr} \Delta_j r \\ &= \Delta_j v - \frac{v}{v^2 - \gamma kT/\mu} \left[ \frac{2\gamma kT}{\mu r} - \frac{\gamma - 1}{\rho v} (\Gamma_{\text{col}} + \Gamma_{\text{lat}}) \right. \\ &\quad \left. - GM/r^2 + 3GM_* r/a^3 \right] \Delta_j r = 0, \end{aligned} \quad (22)$$

$$\begin{aligned} E_{4,j} &\equiv \Delta_j \tau - \frac{d\tau}{dr} \Delta_j r \\ &= \Delta_j \tau + \frac{3}{4s\rho_{\text{int}}} \rho x_{\text{dust}} \Delta_j r = 0. \end{aligned} \quad (23)$$

Note that differences are now computed downwind ( $\Delta_j x \equiv x_{j+1} - x_j$ ), as  $v$  and  $\tau$  have boundary conditions defined at the sonic point ( $j = N$ ). When evaluating variables in (22) and (23), we average across adjacent gridpoints downwind, e.g.,  $\rho \equiv (\rho_j + \rho_{j+1})/2$ .

#### 2.3.2 Boundary Conditions

We need four boundary conditions to solve the system of finite difference equations (20)–(23). At the base of the atmosphere, we set the boundary conditions for gas density and temperature using relations from §2.1:

$$\begin{aligned} E_{1,0} &= \rho_0 - \rho_{\text{vapor}} = 0 \\ E_{2,0} &= T_0 - T_{\text{surface}} = 0. \end{aligned} \quad (24)$$

At our outer boundary — the sonic point — we require the bulk velocity of gas to equal the local sound speed, and  $\tau$  to equal our specified value (§2.2):

$$\begin{aligned} E_{3,N} &= v_N - c_s = 0 \\ E_{4,N} &= \tau_N - \tau_s = 0. \end{aligned} \quad (25)$$

At every step of the iteration we determine  $r_s$  by demanding  $dv/dr$  to be finite at the sonic point. As the denominator of equation (22) vanishes at  $v = c_s$ , we require that

$$\left[ \frac{2\gamma kT}{\mu r} - \frac{\gamma - 1}{\rho v} (\Gamma_{\text{col}} + \Gamma_{\text{lat}}) - \frac{GM}{r^2} + \frac{3GM_* r}{a^3} \right]_{r_s} = 0. \quad (26)$$

#### 2.3.3 Method of Solution

The relaxation method determines the solution by starting with an appropriate guess and iteratively improving it. We use the multi-dimensional Newton’s method as our iteration scheme, which requires us to evaluate partial derivatives of all  $E_{i,j}$  with respect to all  $4N$  dependent variables ( $\rho_j, T_j, v_j, \tau_j$ ). We evaluate partial derivatives numerically, by introducing changes of order  $10^{-8}$  in dependent variables and computing the appropriate finite differences. Newton’s method produces a  $4N \times 4N$  matrix, which we invert using the *numpy* library in *python*. At each iteration we numerically solve equation (26) for  $r_s$  and re-map all  $N$  gridpoints between  $R$  and  $r_s$ . We iterate until variables change by less than one part in  $10^{10}$ .

We found our iteration scheme to be rather fragile. The code only converges if initial guesses are already close to the solution.

For this reason, we started with a simplified version of the problem with a known analytic solution as the initial guess. We then gradually added the missing physics to the code, obtaining a solution with each new physics input until the full problem was solved. Specifically, we began by solving the isothermal Parker wind problem (e.g., Lamers & Cassinelli 1999). We enforced the isothermal condition by declaring  $\gamma$  to be unity, so that our energy equation read  $dT/dr = 0$  (see eq. 21). Additionally, we set  $M_*$  and  $x_{\text{dust}}$  to zero to remove the effects of tidal gravity and dust. We then slowly increased each of the parameters  $M_*$ ,  $\gamma$ , and  $x_{\text{dust}}$  (in that order) to their nominal values. Any subsequent parameter change (e.g.,  $M$ ) was also performed in small increments.

In summary, our code contains three main input parameters:  $x_{\text{dust,amp}}$  and  $x_{\text{dust,max}}$  which prescribe the dust-to-gas profile  $x_{\text{dust}}(r)$ , and the planet mass  $M$ . Our goal is to explore the dependence of the mass loss rate

$$\dot{M} = \Omega \rho v r^2 \quad (27)$$

on these three parameters. Here  $\Omega$  is the solid angle over which the wind is launched, measured from the center of the planet; we set  $\Omega = 1$  since the high surface temperatures required to produce a wind are likely to be reached only near the substellar point. We independently vary the parameters  $x_{\text{dust,max}}$  and  $x_{\text{dust,amp}}$  to find the *maximum*  $\dot{M}$  for a given  $M$ .

### 3 RESULTS

We begin in §3.1 with an isothermal gas model. The isothermal model serves both as a limiting case and as a starting point for developing the full solution which includes a realistic treatment of the energy equation. We provide results for our full model in §3.2. In the full solution we focus on three possible planet masses  $M = 0.01, 0.03$ , and  $0.07 M_{\oplus}$ , finding that  $M \approx 0.01 M_{\oplus}$  yields a *maximum*  $\dot{M}$  that is compatible with the observationally inferred  $\dot{M}_{1255b}$ . We conclude that in the context of our energy equation, the present-day mass of KIC 1255b is *at most*  $\sim 0.02 M_{\oplus}$  (since smaller mass planets can generate still higher  $\dot{M}$  that are also compatible with  $\dot{M}_{1255b}$ ). In §3.3 we integrate back in time to compute the *maximum* formation mass of KIC 1255b.

#### 3.1 Isothermal Solution

We begin by solving a steady, dust-free, isothermal wind described by equations (10) and (11) with  $M_*$  set equal to zero. Although this is a highly idealized problem, its solution provides us with a starting point (i.e., an initial model) from which we are able to solve more complicated problems (see §2.3.3). Our code accepts the standard isothermal wind solution (e.g., Chapter 3 of Lamers & Cassinelli 1999) as an initial guess, with minimal relaxation.

Mass loss rates derived for the isothermal model ( $T=2145$  K, the temperature given by eq. 6 with  $\tau_{\text{surface}} = \tau_s = 0.01$ ) are plotted in Figure 2. They depend strongly on planet mass, with large gains in  $\dot{M}$  for comparatively small reductions in  $M$ , for the basic reason that atmospheric densities are exponentially sensitive to surface gravity. Tidal gravity boosts  $\dot{M}$  by reducing the total effective gravity. As  $M$  decreases, gravity becomes increasingly irrelevant, the thermal speed of the gas eventually exceeds the surface escape velocity, and the dependence of  $\dot{M}$  on  $M$  weakens. In the “free-streaming” limit (dotted lines in Figure 2), mass loss is no longer

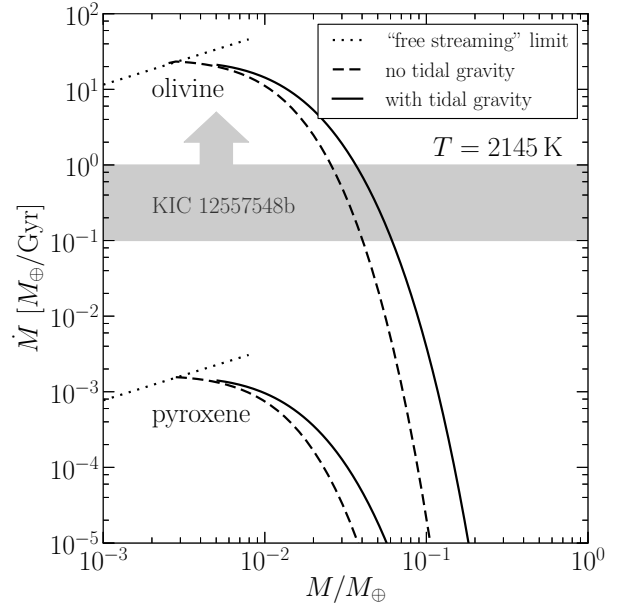


**Figure 2.** Evaporative mass loss rates  $\dot{M}$  vs. planet mass  $M$  for isothermal dust-free winds. Solid lines are for models that include stellar tidal gravity, while dashed curves are for models that do not. As the planet mass is reduced, all solutions converge toward the free-streaming limit where  $\dot{M}$  is not influenced by gravity but instead scales with the surface area of the planet (eq. 28). As inferred from observations, possible present-day mass loss rates  $\dot{M}_{1255b}$  for KIC 1255b are marked in gray. Technically we have only a lower limit on  $\dot{M}_{1255b}$  of  $0.1 M_{\oplus} / \text{Gyr}$ ; for purposes of discussion throughout this paper, we adopt  $0.1\text{--}1 M_{\oplus} / \text{Gyr}$  as our fiducial range (see discussion surrounding equation 5). Clearly KIC 1255b cannot be a pure pyroxene planet. Subsequent figures will refer to planets with pure olivine surfaces (except in §4.7 where we consider iron).

influenced by gravity, and occurs at a rate

$$\dot{M}_{\text{free}} \approx \rho_{\text{vapor}} c_s R^2. \quad (28)$$

Note that  $\dot{M}_{\text{free}}$  decreases when  $M$  is reduced, as less surface area ( $R^2 \propto M^{2/3}$ ) is available for evaporation. For  $M \sim 0.03 M_{\oplus}$ , a pure olivine surface can produce a (dust-free, isothermal) wind for which  $\dot{M}$  becomes compatible with the observationally inferred value for KIC 1255b, on the order of  $\dot{M}_{1255b} \sim 1 M_{\oplus}/\text{Gyr}$  (this is the observed mass loss rate for both dust and gas combined; see our discussion surrounding equation 5 and Rappaport et al. 2012). By contrast, for a pure pyroxene surface,  $\dot{M} \ll \dot{M}_{1255b}$  always. Henceforth we will calculate the density  $\rho_{\text{vapor}}$  of gas at the surface using parameters appropriate for olivine.

#### 3.2 Full Solution

We relax the isothermal condition in our code by slowly increasing  $\gamma$  from 1 to 1.3. With this parameter change, we are solving the full energy equation (eq. 12). Grains are gradually added by modifying  $x_{\text{dust,amp}}$  and  $x_{\text{dust,max}}$ , necessitating the calculation of optical depth (eq. 16).

In Figure 3 we show the solution for which  $\dot{M}$  was maximized (over the space of possible values of  $x_{\text{dust}}$ ) for  $M = 0.03 M_{\oplus}$ , or about half the mass of Mercury. Recall from §3.1 that when the wind was assumed to be isothermal, a planet of this mass was able

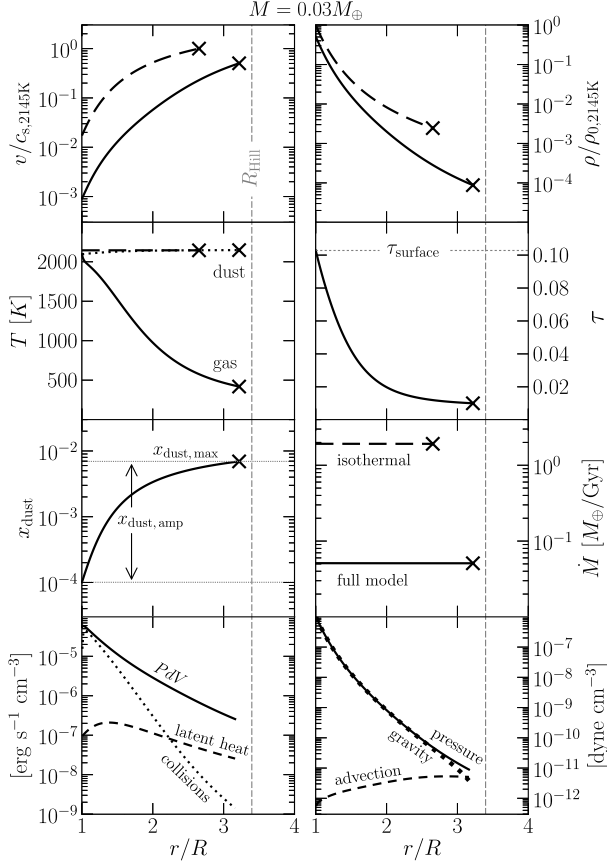


**Figure 3.** Radial dependence of wind properties in the full solution for a planet of mass  $M = 0.03M_{\oplus}$ . Parameters of the  $x_{\text{dust}}$  function are chosen to maximize  $\dot{M}$ . In the upper six panels, the full solution is shown by solid curves, while the dust-free isothermal solution is marked by dashed curves. Values for  $v$  have been normalized to the sound speed at  $T = 2145$  K, and values for  $\rho$  have been normalized to the density  $\rho_{0,2145\text{K}} = \mu P_{\text{vapor}}/(kT)$  evaluated also at  $T = 2145$  K. The  $\times$ -symbol marks the location of the sonic point (the outer boundary of our solution), which occurs close to the Hill radius  $R_{\text{Hill}}$  (marked by a vertical line). The two lower panels show the contributions of the individual terms in the energy and momentum equations (left and right panels, respectively).

to reproduce the inferred mass loss rate of KIC 1255b. Now, with our treatment of the full energy equation and the inclusion of dust,  $\max \dot{M}$  plummets by a factor of 40. Relative to the isothermal solution, the reduction in mass loss rate in the full model is mainly caused by the gas temperature dropping from 2095 K at the planet surface to below 500 K at the sonic point, and the consequent reduction in gas pressure. The temperature drops because gas expands in the wind and does  $PdV$  work. Gas heating by dust-gas collisions or grain formation could, in principle, offset some of the temperature reduction, but having too many grains also obscures the surface from incident starlight, decreasing  $T_{\text{surface}}$  and  $\rho_{\text{vapor}}$  (the latter quantity depends exponentially on the former). The particular dust-to-gas profile  $x_{\text{dust}}$  that is used in Figure 3 is such that the ability of dust to heat gas is balanced against the attenuation of stellar flux by dust, so that  $\dot{M}$  is maximized (for this  $M$ ).

Note that the flow at the base begins with velocities of  $\sim 10^{-3}$  the sound speed. At these subsonic velocities, the atmosphere is practically in hydrostatic equilibrium, with gas pressure and gravity

nearly balancing. Only when velocities are nearly sonic does advection become a significant term in the momentum equation (bottom right panel of Figure 3). Flow speeds are still high enough at the base of the atmosphere to lift dust grains against gravity for all but the highest planet masses considered (§4.2; gas speeds as low as  $\sim 1$  m/s in a  $\sim 1 \mu\text{bar}$  atmosphere can enable micron-sized grains to escape sub-Mercury-sized planets, as can be verified by equation 30; furthermore, the condition that grains not slip relative to gas is conveniently independent of gas velocity in the Epstein free-molecular drag regime, as can be seen in equation 29. Our flows are entirely in the Epstein drag regime, as explained below equation 29.)

In Figure 4, we show how  $\dot{M}$  and  $\tau_{\text{surface}}$  vary with the function  $x_{\text{dust}}$ . As just discussed,  $\max \dot{M}$  is reached for a specific choice of parameters which balance gas heating by dust and surface obscuration by dust. (We emphasize, here and elsewhere, that we have not identified a physical reason why actual systems like KIC 1255b should have mass loss rates  $\dot{M}$  that equal their theoretically allowed maximum values.) Apart from the region near the peak in  $\dot{M}$ , contours of constant  $\tau_{\text{surface}}$  are roughly parallel to contours of constant  $\dot{M}$ , suggesting that the value of  $\tau_{\text{surface}}$  is more important for determining  $\dot{M}$  than the specific functional form of  $x_{\text{dust}}$ . This finding increases the confidence we have in the robustness of our solution.

It is clear from Figures 3 and 4 that a planet of mass  $M = 0.03 M_{\oplus}$  can only emit winds for which  $\max \dot{M} < \min \dot{M}_{1255b} \sim 0.1 M_{\oplus} / \text{Gyr}$  (at least within the context of our energy equation). In Figure 5 we show results for  $M = 0.01 M_{\oplus}$ , for which  $\max \dot{M} > \min \dot{M}_{1255b}$ . For this  $M$ , the mass loss rate  $\dot{M}$  is maximized when the planet surface is essentially unobscured by dust. At our arbitrarily chosen value for  $x_{\text{dust}} \sim 3 \times 10^{-7}$ , the wind is not significantly heated by dust and expands practically adiabatically. The maximum  $\dot{M}$  is reached for an essentially dust-free solution because the wind is blowing at too high a speed for dust-gas collisions to be important. That is, the timescale over which gas travels from the planet’s surface to the sonic point is shorter than the time it takes a gas particle to collide with a dust grain; gas is thermally decoupled from dust. Were we to increase  $x_{\text{dust}}$  to make dust-gas heating important, the flow would become optically thick and the wind would shut down. If the model shown in Figure 5 does represent KIC 1255b, then the dust grains that occult the star must condense outside the sonic point, beyond the Hill sphere.

Figure 6 shows the solution for  $M = 0.07 M_{\oplus}$ . In this case  $\dot{M}$  is maximized when enough dust is present to heat the gas significantly above the adiabat. At this comparatively large planet mass, initial wind speeds are low enough that a gas particle collides many times with dust over the gas travel time, so that dust-gas collisions heat the gas effectively near the surface of the planet. Further downwind, near the sonic point, latent heating overtakes  $PdV$  cooling and actually increases the temperature of the gas with increasing altitude. The wind is much more sensitive to heating near the base of the flow than near the sonic point: if we omit latent heating from our model — so that gas cools to  $\sim 500$  K at the sonic point — then  $\dot{M}$  is reduced by only a factor of two. In comparison,  $\dot{M}$  drops by several orders of magnitude if dust-gas collisions are omitted.

The dependence of  $\dot{M}$  on  $x_{\text{dust}}$  in both the “dust-free low-mass” and the “dusty high-mass” limits is illustrated in Figure 7. In the low-mass limit,  $\dot{M} = \max \dot{M}$  when no dust is present. In this regime, gas moves too quickly for heating by dust to be significant; dust influences the flow only by attenuating starlight, and as long as  $\tau_{\text{surface}} \ll 1$ , dust hardly affects  $\dot{M}$ . By contrast, in the high-mass limit,  $\dot{M} = \max \dot{M}$  for the dustiest flows we consider (i.e., the high-

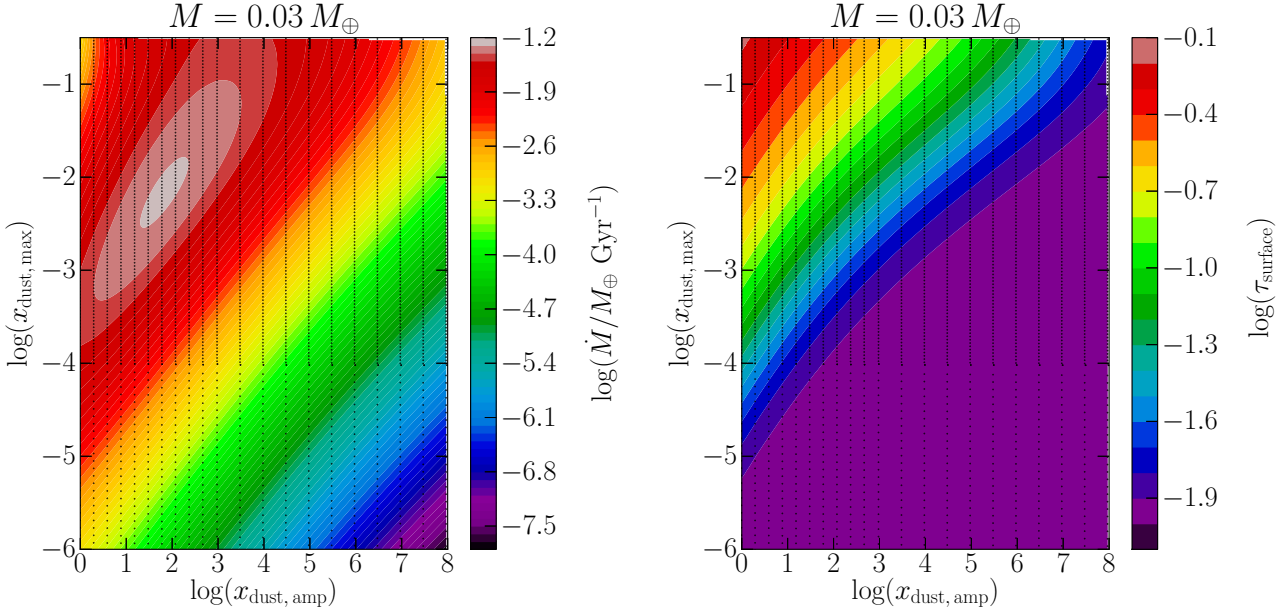


**Figure 4.** *Left panel:* Dependence of  $\dot{M}$  on dust abundance for a planet of mass  $M = 0.03 M_{\oplus}$ . The dust abundance parameters  $x_{\text{dust, max}}$  and  $x_{\text{dust, amp}}$  are defined in equation (19); see also Figure 3. Both parameters are varied independently to find the maximum  $\dot{M}$ , which occurs at  $\log(x_{\text{dust, amp}}, x_{\text{dust, max}}) \sim (1.7, -2.2)$ . The full model corresponding to this maximum  $\dot{M}$  is detailed in Figure 3. Each black dot corresponds to a full model solution. Colour contours for  $\dot{M}$  are interpolated using a cubic polynomial. *Right panel:* Optical depth  $\tau_{\text{surface}}$  between the star and the planetary surface as a function of dust abundance for a planet of mass  $M = 0.03 M_{\oplus}$ . Apart from the region near the peak in  $\dot{M}$ , contours of constant  $\tau_{\text{surface}}$  are roughly parallel to contours of constant  $\dot{M}$ , suggesting that the value of  $\tau_{\text{surface}}$  is more important for determining  $\dot{M}$  than the specific functional form of  $x_{\text{dust}}$ .

est values of  $x_{\text{dust, max}}$ ). In this regime,  $\dot{M}$  is very sensitive to dust abundance, with values spanning six orders of magnitude over the explored parameter space.

In Figure 8 we show mass loss rates as a function of planet mass for the full model. We emphasize that these are maximum mass loss rates, found by varying  $x_{\text{dust}}$ . At low planet masses,  $\max \dot{M}$  for the full model converges with  $\dot{M}$  for the isothermal model because both approach the free-streaming limit, where gravity becomes irrelevant and  $\dot{M}$  is set entirely by conditions at the surface of the planet (eq. 28). To reach  $\dot{M}_{1255b} > 0.1 M_{\oplus} / \text{Gyr}$ , the present-day mass of KIC 1255b must be  $\lesssim 0.02 M_{\oplus}$ , or less than about twice a lunar mass.

We have verified *a posteriori* for the models shown in Figures 3, 5, and 6 that the sonic point is attained at an altitude where the collisional mean free path of gas molecules is smaller than  $r_s$ , so that the hydrodynamic approximation embodied in equations (10)–(12) is valid. In other words, the exobase lies outside the sonic point in these  $\dot{M} = \max \dot{M}$  models. The margin of safety is largest for the lowest mass models.

### 3.3 Mass-Loss Histories

We calculate mass-loss histories  $M(t)$  by time-integrating our solution, shown in Figure 8, for  $\max \dot{M}(M)$ . Before we integrate, however, we introduce  $0 < f_{\text{duty}} < 1$  to account for the duty cycle of the wind: we define  $f_{\text{duty}} \cdot \max \dot{M}$  as the time-averaged mass-loss rate. We estimate that  $f_{\text{duty}} \sim 0.5$  based on the statistics of transit depths compiled by Brogi et al. (2012, see their figure 2). We time-integrate  $f_{\text{duty}} \cdot \max \dot{M}$  to obtain the  $M(t)$  curves shown in Figure 9.

(This factor of 2 correction for the duty cycle should not obscure the fact that the actual mass loss rate, time-averaged or otherwise, could still be much lower than the theoretically allowed  $\max \dot{M}$ , a possibility we return to throughout this paper.)

We highlight the case of a planet with a lifetime of  $t_{\text{life}} = 5$  Gyr. Under our full (non-isothermal) model (right panel of Figure 9), such a planet has a mass at formation of  $0.06 M_{\oplus}$  and gradually erodes over several Gyr until it reaches  $M \sim 0.03 M_{\oplus}$  — whereupon the remaining mass is lost catastrophically over a short time (just how short is estimated for the specific case of KIC 1255b below). Contrast this example with planets having initial masses  $\gtrsim 0.07 M_{\oplus}$  — these have such low  $\dot{M}$  that they barely lose any mass over Gyr timescales.

For comparison, we also present mass-loss histories using a dust-free isothermal model with stellar tidal gravity (left panel of Figure 9). Compared to our non-isothermal solutions — for which gas temperatures fall immediately as the wind lifts off the planet surface — the isothermal solution corresponds to a flow which stays relatively pressurized and which therefore enjoys the largest  $\dot{M}$  for a given  $M$ . The isothermal wind thus represents an endmember case. However, the mass-loss histories under the isothermal approximation do not differ qualitatively from those using the full energy equation. For isothermal winds, the dividing mass between planet survival and destruction within 10 Gyr is about  $0.11 M_{\oplus}$ , only  $\sim 40\%$  larger than the value cited above for our non-isothermal solutions.



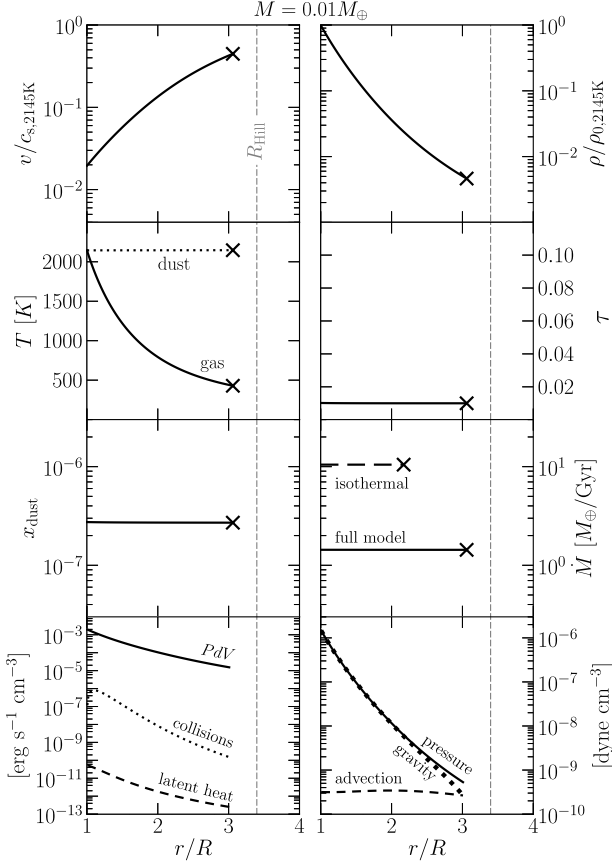


**Figure 5.** Same as Figure 3, but for a planet of mass  $M = 0.01 M_{\oplus}$ . For this planet mass,  $\dot{M}$  is maximized when essentially no dust is present (i.e., the atmosphere is essentially transparent) as gas moves too quickly for dust-gas collisions to heat the gas. As such, all heating terms are negligible and the gas expands adiabatically.

### 3.4 Possible Mass Loss Histories for KIC 1255b

Figures 8 and 9 can be used to sketch possible mass-loss histories for KIC 1255b. For our first scenario, we employ the full model that solves the full energy equation. Today, to satisfy the observational constraint that  $\dot{M}_{1255b} > 0.1 M_{\oplus}/\text{Gyr}$  (see the derivation of our equation 5), the planet must have a present-day mass of *at most*  $M \approx 0.02 M_{\oplus}$ , or roughly twice the mass of the Moon (Figure 8). Such a low mass implies that currently KIC 1255b is in a “catastrophic evaporation” phase (vertical straight lines in Figure 9). Depending on the age of the planet (i.e., the age of the star: 1–10 Gyr), KIC 1255b originally had a mass of *at most* 0.04–0.07  $M_{\oplus}$ : 2–4 times its maximum current mass, or about the mass of Mercury. Starting from today, the time the planet has before it disintegrates completely is on the order of  $t_{\text{evap}} \sim M/(f_{\text{duty}} \cdot \max \dot{M})$ , which is as long as 400 (40) Myr for  $M = 0.02 M_{\oplus}$ ,  $f_{\text{duty}} = 0.5$ , and  $\max \dot{M} = 0.1 (1) M_{\oplus}/\text{Gyr}$ .

If our energy equation were somehow in error and the wind better described as isothermal, then the numbers cited above would change somewhat. The present-day mass of KIC 1255b would be at most  $M \sim 0.07 M_{\oplus}$ ; the maximum formation mass would be between 0.08–0.11  $M_{\oplus}$ ; and the evaporation timescale starting from

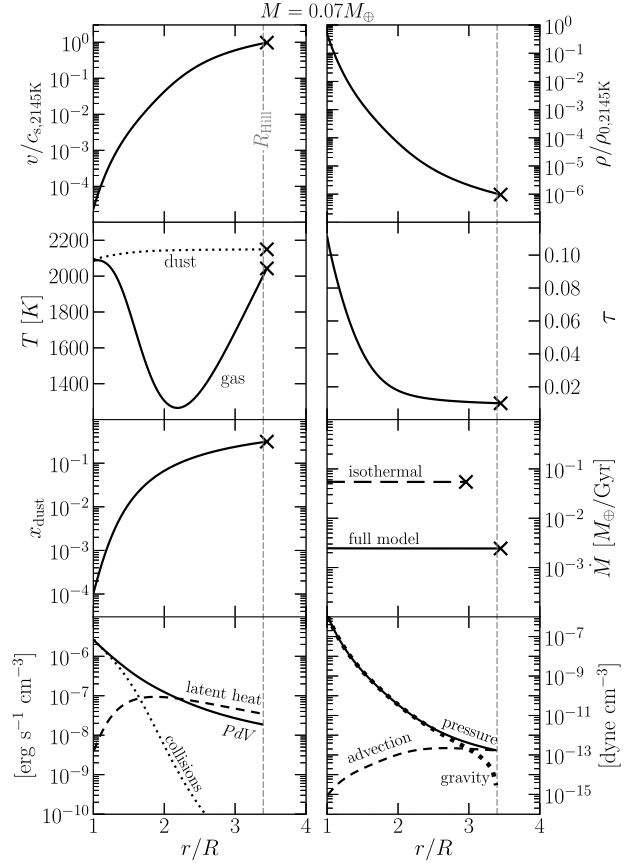


**Figure 6.** Same as Figure 3, but for a planet of mass  $M = 0.07 M_{\oplus}$ . For this mass,  $\dot{M}$  is maximized for the dustiest flows considered in this paper. The outflow is launched at such low velocities that collisional dust-gas heating is important. Near the sonic point, latent heating overtakes  $PdV$  cooling and the temperature of the gas rises.

today could be as long as  $t_{\text{evap}} \sim 400$  Myr if the present-day mass  $M \sim 0.07 M_{\oplus}$ .

As we have stressed throughout, a critical assumption we have made is that the time-averaged mass loss rate is  $f_{\text{duty}} \cdot \max \dot{M}$  with  $f_{\text{duty}}$  as high as 0.5. We have not identified a physical reason why the actual mass loss rate should be comparable to the theoretically allowed  $\max \dot{M}$  for a given  $M$ . If our assumption were in error and actual mass loss rates  $\dot{M} \ll \max \dot{M}$ , then the present-day mass of KIC 1255b, the corresponding evaporation time, and the formation mass of KIC 1255 would all decrease from the upper bounds cited above.

The degeneracy of possible masses and evaporative histories outlined in this section could be broken with observational searches for the progenitors of KIC 1255b-like objects (§4.6).

## 4 DISCUSSION

We discuss how mass loss is not “energy-limited” in §4.1; how gas entrains dust in §4.2; how the evaporative wind can be time-variable in §4.3; the effects of winds on orbital evolution in §4.4; the interaction of the planetary wind with the stellar wind in §4.5; the occurrence rate of quiescent progenitors of catastrophically

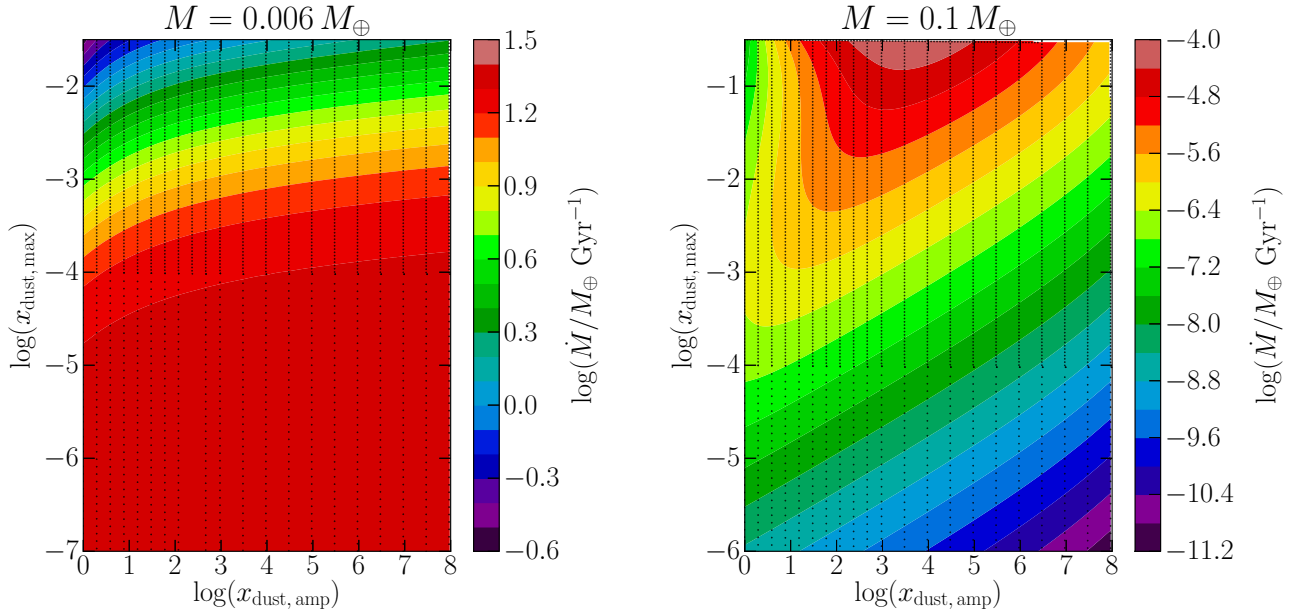


**Figure 7.** *Left panel:* Same as the left panel of Figure 4, but for a planet of mass  $M = 0.006 M_{\oplus}$ . In this low-mass limit,  $\dot{M}$  is maximized when no dust is present (i.e., when the atmosphere is transparent) because gas is moving too quickly for heating by dust to be significant. *Right panel:* Same as left panel, but for a planet of mass  $M = 0.1 M_{\oplus}$ . In this high-mass limit,  $\dot{M}$  is maximized for the dustiest flows we consider (i.e., the highest values of  $x_{\text{dust,max}}$ ) because flow speeds near the surface are slow enough for dust-gas energy exchange to be significant.

evaporating planets in §4.6; the possibility that evaporating planets can be naked iron cores in §4.7; and the ability of dust to condense out of the wind in §4.8.

#### 4.1 Mass Loss is Not Energy-Limited

Atmospheric mass loss rates are commonly assumed to be “UV-energy-limited”: it is assumed that a fixed, order-unity fraction  $\epsilon$  of the incident UV flux  $F_{\text{UV}}$  does  $PdV$  work and lifts material out of the planet’s gravitational well. Under the energy-limited assumption, the mass loss rate is  $\dot{M} \sim \epsilon \pi R^2 F_{\text{UV}} / (GM/R)$ . The validity of this formula has been tested by Watson et al. (1981) for terrestrial atmospheres and by Murray-Clay et al. (2009) for hot Jupiters.

The energy-limited formula does not apply at all to the evaporating rocky planets considered in this paper. The stellar UV flux is not essential for low-mass planets because their escape velocities are so small that energy deposition by photoionization is not necessary for driving a wind. Even optical photons — essentially the stellar bolometric spectrum — can vaporize close-in planets. Merely replacing  $F_{\text{UV}}$  with  $F_{\text{bolometric}}$  in the energy-limited formula would still be misleading, however, because most of the incident energy is radiated away and does no mechanical work. More to the point,  $\epsilon$  is not constant; as discussed in §3.2, the energetics of the flow changes qualitatively with planet mass. If we were to insist on using the energy-limited formula, we would find  $\epsilon \sim 10^{-8}$  for  $M \sim 0.1 M_{\oplus}$ , and  $\epsilon \sim 10^{-4}$  for  $M \sim 0.01 M_{\oplus}$  (see Figure 8).

#### 4.2 Dust-Gas Dynamics

In our model we have assumed that dust grains condensing within the wind are carried along without any relative motion between dust

and gas (1-fluid approximation). Grains are well entrained if their momentum stopping times

$$t_{\text{stop}} \sim \frac{m_{\text{grain}} v_{\text{rel}}}{\rho v_{\text{rel}} c_s s^2} \sim \frac{s \rho_{\text{int}}}{\rho c_s} \quad (29)$$

are shorter than the grain advection time  $t_{\text{adv}} \sim R/v$ . In equation (29),  $m_{\text{grain}}$  is the mass of an individual grain and  $v_{\text{rel}}$  is the relative gas-grain velocity. The aerodynamic drag force in the denominator is given by the Epstein law, which is appropriate for  $v_{\text{rel}} \lesssim c_s$  and grain sizes  $s$  smaller than the gas collisional mean free path (for our flows,  $\lambda_{\text{mfp}} \sim \mu/(\rho\sigma) \gtrsim 2$  cm, where  $\sigma \sim 3 \times 10^{-15}$  cm<sup>2</sup>).

We find using our full model (for  $\dot{M} = \max \dot{M}$ ) that  $t_{\text{stop}}/t_{\text{adv}} < 1$  everywhere for  $M < 0.03 M_{\oplus}$ , confirming our assumption that micron-sized (and smaller) grains are well-entrained in the winds emanating from such low-mass planets. When  $M = 0.03 M_{\oplus}$ ,  $t_{\text{stop}} < t_{\text{adv}}$  close to the planet’s surface, but as gas nears the sonic point,  $t_{\text{stop}}$  becomes comparable to  $t_{\text{adv}}$ . For  $M > 0.03 M_{\oplus}$ , the 1-fluid approximation breaks down near the sonic point. For such large planet masses, future models should account for gas-grain relative motion — in addition to other effects that become increasingly important near the sonic point / Hill sphere boundary (e.g., Coriolis forces and stellar radiation pressure). Note that the 1-fluid approximation should be valid for the present-day dynamics of KIC 1255b, since according to the full model its current mass is at most  $M \approx 0.02 M_{\oplus} < 0.03 M_{\oplus}$ .

Although dust can slip relative to gas, dust can still be transported outward and escape the planet if the aerodynamic drag force exceeds the force of gravity:

$$\rho v_{\text{rel}} c_s s^2 \gtrsim \rho_{\text{int}} s^3 g, \quad (30)$$

where  $g = G(M/r^2 - 3M_*r/a^3)$  is the total gravitational acceleration. Grains that manage to be lifted beyond the Hill sphere (which

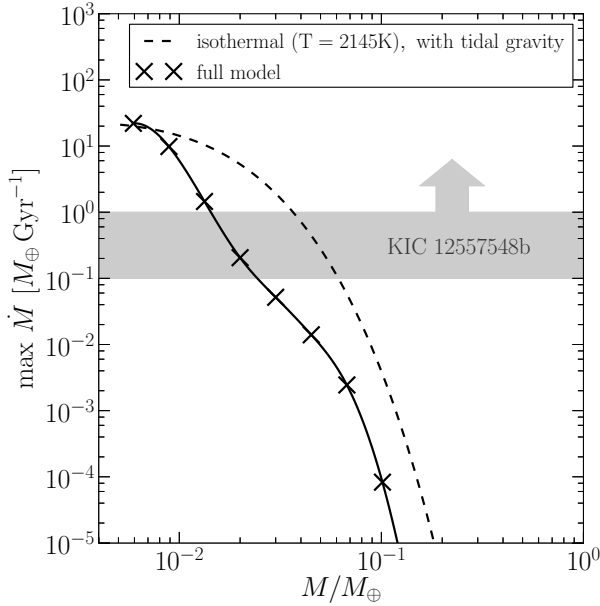


**Figure 8.** Maximum mass loss rates  $\dot{M}$  vs. planet mass  $M$  for the full model. At each  $\times$ -marked mass,  $\max \dot{M}$  was found by varying  $x_{\text{dust}}$  as described, e.g., in Figure 4. The solid curve is a cubic spline interpolation. Mass loss rates for the full model are generally lower than for the isothermal model (dashed curve) because the dust-gas heating terms we have included in our full model turn out to be inefficient. At low planet masses, the isothermal and full models converge because both approach the free-streaming limit, where gravity becomes irrelevant and  $\dot{M}$  is set entirely by conditions at the surface (i.e., surface area, equilibrium vapor pressure, and sound speed; eq. 28). According to the full model, the present-day mass of KIC 1255b is  $\leq 0.02 M_{\oplus}$ , or less than twice the mass of the Moon; for such masses,  $\max \dot{M} > \min \dot{M}_{1255b} \sim 0.1 M_{\oplus} / \text{Gyr}$ .

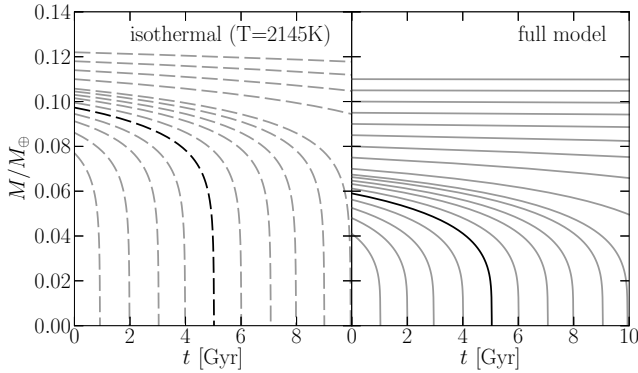


**Figure 9.** Mass-loss histories  $M(t)$  obtained by time-integrating  $f_{\text{duty}} \cdot \max \dot{M}(M)$  with  $f_{\text{duty}} = 0.5$  for the isothermal and full models. We highlight the case of a planet with a 5 Gyr lifetime. For the full model (right panel), this corresponds to an initial mass of  $\sim 0.06 M_{\oplus}$ , slightly larger than the mass of Mercury. Such a planet could have formed *in situ* and slowly eroded over several Gyr until reaching  $\sim 0.03 M_{\oplus}$ , whereupon the planet evaporates completely in a few hundred Myr. By contrast, planets with formation masses  $\geq 0.07 M_{\oplus}$  survive (in the full model) for tens of Gyrs with-out significant mass loss.

is situated close to the sonic point in all our models) are no longer bound to the planet. Outside the Hill sphere, dust decouples from gas and is swept into a comet-like tail by stellar radiation pressure and Coriolis forces.

For  $M \approx 0.03 M_{\oplus}$  and our adopted grain size  $s = 1 \mu\text{m}$ , the forces in equation (30) are comparable near the sonic point when  $v_{\text{rel}} \sim c_s$  (i.e., when grains are barely lifted by drag). For  $M > 0.03 M_{\oplus}$ , micron-sized and larger grains will not be dragged past the sonic point according to (30) — thus our assumption that they do fails for such high-mass planets, and will need to be rectified in future models. Smaller, sub-micron-sized grains can, however, be lifted outward. Moreover, sub-micron sized grains may heat the gas more effectively because they have greater geometric surface area for dust-gas collisions (at fixed  $x_{\text{dust}}$ ) and because their temperatures exceed those of blackbodies (their efficiencies for emission at infrared wavelengths are much less than their absorption efficiencies at optical wavelengths). The superior momentum and thermal coupling enjoyed by grains having sizes  $s \ll 1 \mu\text{m}$ , plus their relative transparency at optical wavelengths — which helps them avoid shadowing the planet surface from stellar radiation — motivate their inclusion in the next generation of models.

Our model could be improved still further by self-consistently accounting for how the gas density  $\rho$  must decrease as dust grains condense out of gas. Moreover, the restriction that  $x_{\text{dust}} < 1$  could be lifted.

### 4.3 Time Variability

Occultations of KIC 12557548 vary in depth from a maximum of 1.3% to a minimum of  $\leq 0.2\%$  on orbital timescales. Rappaport et al. (2012) discussed qualitatively the possibility that such transit depth variations arise from a limit cycle that alternates between high- $\dot{M}$  and low- $\dot{M}$  phases. A high- $\dot{M}$  phase that produces a deep eclipse would also shadow the planet surface from starlight. The resultant cooling would lower the surface vapor pressure and lead to a low- $\dot{M}$  phase — after which the atmosphere would clear, the surface would re-heat, and the cycle would begin anew. Such limit cycle behavior could be punctuated by random explosive events that release dust, similar to those observed on Io (Geissler 2003; see also the references in §4.2 of Rappaport et al. 2012).

Order-of-magnitude variations in  $\dot{M}$  arise from only small fractional changes in surface temperature because the vapor pressure of gas over rock depends exponentially on temperature. For example, from equations (6) and (7), we see that increasing the surface optical depth  $\tau_{\text{surface}}$  from 0.1 to 0.4 reduces the surface temperature  $T_{\text{surface}}$  by 150 K and the base density  $\rho_{\text{vapor}}$  by a factor of 10. Such changes would cause  $\dot{M}$  to drop by more than a factor of 10, because  $\dot{M}$  scales super-linearly with  $\rho_{\text{vapor}}$ : a linear dependence results simply because  $\dot{M}$  scales with gas density, while an additional dependence arises because the wind speed increases with the gas pressure gradient, which in turn scales as  $\rho_{\text{vapor}} T_{\text{surface}}$ .

To reproduce the orbit-to-orbit variations in transit depth observed for KIC 1255b, the dynamical time  $t_{\text{dyn}}$  of the wind cannot be much longer than the planet’s orbital period of  $P_{\text{orb}} = 15.7 \text{ hr}$ . The dynamical time is that required for dust to be advected from the planet surface to the end of the comet-like tail that occults the star: it is the minimum timescale over which the planet’s transit signature “refreshes”. If  $t_{\text{dyn}} \gg P_{\text{orb}}$ , then we would expect transit

depths to be correlated from one orbit to the next — in violation of the observations.

Referring to the full model for a KIC 1255b-like mass of  $M \approx 0.01 M_{\oplus}$  (Figure 5), we estimate that

$$t_{\text{dyn}} = \int_R^{r_s} \frac{dr}{v} + \int_{r_s}^{0.1R_*} \frac{dr}{v} \sim 13 \text{ hr} + \frac{0.1R_*}{v_2} \sim 14 \text{ hr}, \quad (31)$$

where we have split  $t_{\text{dyn}}$  into two parts: the first integral is the time for dust to reach the sonic point (the outer boundary of our calculation), while the second integral is the time for dust to travel out to  $0.1R_*$  (a circular, optically disk of this radius would generate a 1% transit depth). The first integral is performed numerically using our full model (upper left panel of Figure 5), while the second integral is estimated to order-of-magnitude using a characteristic grain velocity (well outside the planet’s Hill sphere) of  $v_2 \sim 10 \text{ km s}^{-1}$  (Rappaport et al. 2012; see their equation 6 and related commentary). Since  $t_{\text{dyn}} \lesssim P_{\text{orb}}$ , we conclude that the wind/cometary tail can refresh itself quickly enough to change its appearance from orbit to orbit.

We can go one step further. The timescale over which  $\dot{M}$  changes should be the timescale over which the stellar insolation at the planetary surface changes — in other words, the timescale over which the “weather” at the substellar point, where the wind is launched, changes from, e.g., “overcast” to “clear”. Ignoring the possibility of volcanic eruptions, we estimate this variability timescale as the time for the wind to reach the Hill sphere boundary, at which point the Coriolis force has turned the wind by an order-unity angle away from the substellar ray joining the planet to the star (i.e., beyond the Hill sphere, the dust-laden wind no longer blocks stellar radiation from hitting the substellar region where the wind is launched). Because the Hill radius is situated near the sonic point, this variability timescale is given approximately by the first integral in equation (31):  $t_{\text{dyn}}^a \approx 13 \text{ hr}$ .

The fact that  $t_{\text{dyn}}^a$  is neither much shorter than nor much longer than  $P_{\text{orb}}$  supports our proposal that the observed time variability of KIC 1255b is driven by a kind of limit cycle involving stellar insolation and mass loss. Clearly if  $t_{\text{dyn}}^a \gg P_{\text{orb}}$ , orbit-to-orbit variations in  $\dot{M}$  would be impossible. Conversely, if  $t_{\text{dyn}}^a \ll P_{\text{orb}}$  — or more precisely if  $t_{\text{dyn}}^a$  were much shorter than the transit duration of 1.5 hr — then the wind would vary so rapidly that each transit observation would time-integrate over many cycles, yielding a smeared-out average transit depth that would not vary from orbit to orbit as is observed.

#### 4.4 Long-Term Orbital Evolution

When computing planet lifetimes in §3.3, we have assumed that the planet does not undergo any orbital evolution while losing mass. This approximation is valid because gas leaves the planet’s surface at velocities  $v_{\text{launch}} \lesssim c_s \sim 1 \text{ km s}^{-1}$ . Launch velocities are so low compared to the orbital velocity of the planet  $v_{\text{orb}} \sim 200 \text{ km s}^{-1}$  that the total momentum imparted by the wind is a tiny fraction of the planet’s orbital momentum.

We quantify this as follows. We estimate the total change in semimajor axis  $a$  and eccentricity  $e$  from Gauss’ equations (see, e.g., Murray & Dermott 1999). Consider the case in which the gas is launched at a velocity  $v_{\text{launch}}$  at an angle  $\alpha$  from the substellar ray and in the plane of the planet’s orbit. The angle  $\alpha$  could be non-zero because of surface inhomogeneities or asynchronous rotation

of the planet. Neglecting terms of order  $e^2$  and  $\alpha e$ , we find that  $a$  and  $e$  evolve according to

$$\begin{aligned} \frac{da}{dt} &\sim a \frac{v_{\text{launch}}}{v_{\text{orb}}} \frac{\dot{M}}{M} (e + \alpha), \\ \frac{de}{dt} &\sim \frac{v_{\text{launch}}}{v_{\text{orb}}} \frac{\dot{M}}{M} (1 + \alpha), \end{aligned} \quad (32)$$

where the first term in parentheses on the right-hand-side of each equation is due to the radial component of the perturbation and the second term is due to the azimuthal component (where radius and azimuth are measured in a cylindrical coordinate system centered at the star and in the plane of the planet’s orbit). Integrating equations (32) yields the changes in  $a$  and  $e$  accumulated over the planet’s age:

$$\begin{aligned} \frac{\Delta a}{a} &\sim \ln \left( \frac{M_{\text{initial}}}{M_{\text{final}}} \right) \frac{v_{\text{launch}}}{v_{\text{orb}}} (e + \alpha) \lesssim 0.01 (e + \alpha), \\ \Delta e &\sim \ln \left( \frac{M_{\text{initial}}}{M_{\text{final}}} \right) \frac{v_{\text{launch}}}{v_{\text{orb}}} \lesssim 0.01. \end{aligned} \quad (33)$$

When evaluating equation (33), we have used the maximum possible launch velocity  $v_{\text{launch}} \sim c_s$  (valid in the “free-streaming” limit) and  $M_{\text{initial}}/M_{\text{final}} \sim 5$  (see §3.3).

The fact that evaporating planets undergo negligible orbital evolution suggests they could have resided on their current orbits for Gyrs — indeed they might even have formed *in situ*. Swift et al. (2013) would disfavor *in-situ* formation of KIC 1225b because at the planet’s orbital distance, dust grains readily sublimate, and ostensibly there would have been no solid material in the primordial disk out of which rocky planets could have formed. However, a less strict *in-situ* formation scenario is still viable. Solid bodies larger than dust grains obviously have longer evaporation times. Such large planetesimals could have drifted inward through the primordial gas disk and then assembled into the progenitors of objects like KIC 1255b at their current close-in distances (e.g., Youdin & Shu 2002; Hansen & Murray 2012; Chiang & Laughlin 2013). Solid particles can avoid vaporization if they merge faster than they evaporate.

#### 4.5 Flow Confinement by Stellar Wind

When computing the transonic solution for the planetary wind, we implicitly assumed that the outflow was expanding into a vacuum. In reality, the outflow from the planet will collide with the stellar wind and form a “bubble” around the planet.<sup>2</sup> For our solution to be valid, the radius of the bubble — i.e., the surface of pressure balance between the winds — has to be downstream of the sonic point where the flow is supersonic. This way, any pressure disturbance created at the interface cannot propagate upstream and influence our solution.

At the wind-wind interface, the normal components of the pressures of the planetary and stellar winds balance. The total pressure includes the ram, thermal, and magnetic contributions. We compare the pressure of the stellar wind at  $a \sim 0.01 \text{ AU} \sim 4R_*$

<sup>2</sup> The considerations in this section parallel those for hot Jupiter winds and their bow shocks; see Tremblin & Chiang (2013), Vidotto et al. (2010, 2011a,b), and Llama et al. (2011).



with that of the planetary wind computed at  $r_s$  to gauge whether the interface occurs downstream of  $r_s$ . For the pressure  $P_*$  of a main-sequence, solar-type star we are guided by the Solar wind. Flow speeds of the Solar wind are measured by tracking the trajectories of coronal features (Sheeley et al. 1997; Quémerais et al. 2007). At  $a = 0.01$  AU the Solar wind<sup>3</sup> is still accelerating with typical flow speeds of  $v_* \sim 100$  km s<sup>-1</sup>. For this  $v_*$ , and a canonical Solar mass-loss rate of  $2 \times 10^{-14} M_\odot$  yr<sup>-1</sup>, the proton number density is  $n_* = 2 \times 10^5$  cm<sup>-3</sup>. We take the proton temperature to be  $T_* \sim 10^6$  K (Sheeley et al. 1997) and the heliospheric magnetic field strength to be  $B_* \approx 0.1$  G at 0.01 AU (Kim et al. 2012). The total stellar pressure at 0.01 AU is then  $P_* \sim n_* m_H v_*^2 + n_* k T_* + B_*^2 / (8\pi) \sim 4 \times 10^{-4}$  dyne cm<sup>-2</sup>, with the magnetic pressure dominating other terms by an order of magnitude.

The ram and thermal pressures of the planet’s wind are equal at the sonic point and add up to (for  $\dot{M} = \max \dot{M}$ )  $P_s \sim 2 \times 10^{-3}$  ( $1 \times 10^{-4}$ ) dyne cm<sup>-2</sup> when  $M = 0.03$  (0.07)  $M_\oplus$ . Thus for  $M \leq 0.03 M_\oplus$  (a range that includes possible present-day masses of KIC 1255b),  $P_s > P_*$  so that the planetary wind blows a bubble that extends beyond the sonic point and the transonic solutions we have computed are self-consistent. By contrast for  $M \sim 0.07 M_\oplus$ ,  $P_s \sim P_*/4 < P_*$  so that the stellar wind pressure will balance the planetary wind pressure inside of  $r_s$ . The stellar wind will prevent the planetary wind from reaching supersonic velocities; the planetary outflow will conform to a “breeze” solution with a reduced  $\dot{M}$ . If the colliding winds in our problem behave like those of hot Jupiters and their host stars, then  $P_s \sim P_*/4$  will reduce  $\dot{M}$  by  $\sim 30\%$  (see figure 12 of Murray-Clay et al. 2009).

We have found  $P_*$  to be dominated by magnetic pressure. Since magnetic fields only interact with the ionized component of the planetary wind, and since the planetary wind may not be fully ionized, we might be over-estimating the effect of  $P_*$ . Dust grains in the planetary wind may absorb free charges so that the wind may be too weakly ionized to couple with the stellar magnetic field. If we ignore the magnetic contribution to the stellar wind, then  $P_s > P_*$  for all planet masses that we have considered, and all our transonic solutions would be self-consistent.

What about the planet’s magnetic field? A sufficiently ionized outflow could be confined by the planet’s own magnetic field. To assess the plausibility of this scenario, we use Mercury’s field as a guide for KIC 1255b. The flyby of *Mariner 10* and recent measurements by *MESSENGER* show that Mercury possesses a weak magnetic field with a surface strength of  $\sim 3 \times 10^{-3}$  Gauss (Ness et al. 1974; Anderson et al. 2008). The associated magnetic pressure  $\sim 4 \times 10^{-7} (R/r)^6$  dyne cm<sup>-2</sup> is small compared to both the thermal pressures that we have computed at the planet surface and the hydrodynamic pressures at the sonic point. For planetary magnetic fields to confine the wind, they are required to have surface strengths in excess of  $\sim 30$  Gauss.

<sup>3</sup> These stellar wind parameters are appropriate for the “slow” Solar wind blowing primarily near the equatorial plane of the Sun. In addition, the Solar wind also contains a “fast” component which emerges from coronal holes. During Solar minimum, the fast Solar wind is confined mainly to large heliographic latitudes, but may reach the equator plane during periods of increased solar activity (Kohl et al. 1998; McComas et al. 2003). Because most planets are expected to orbit near their stellar equatorial planes, we take the slow component of the Solar wind to be a better guide.

#### 4.6 Occurrence Rates of Close-In Progenitors

According to our analysis in §3.4, currently KIC 1255b has a mass of at most 0.02–0.07  $M_\oplus$ , and is in a final, short-lived, catastrophically evaporating phase possibly lasting another  $t_{\text{evap}} \sim 40$ –400 Myr during which dust is ejected at a large enough rate to produce eclipse depths of order 1%. But for most of its presumably Gyrs-long life, KIC 1255b was a more quiescent planet — larger but still less than roughly Mercury in size (§3.4), with a stronger gravity and emitting a much more tenuous wind. We therefore expect that for every KIC 1255b-like object discovered, there are many more progenitors in the quiescent phase — i.e., planets having sizes up to about that of Mercury orbiting main sequence K-type stars at  $\sim 0.01$  AU.

Out of the  $\sim 45,000$  main sequence K-type stars in the Kepler Input Catalogue (Batalha et al. 2010), there is apparently only 1 object like KIC 1255b. Then

$$f_{\text{observed}} \sim f_{\text{progenitor}} f_{\text{transit}} f_{\text{evap}} \sim \frac{1}{45000}, \quad (34)$$

where  $f_{\text{progenitor}}$  is the intrinsic occurrence rate of progenitors around K stars with orbital periods shorter than a day,  $f_{\text{transit}} \sim R_*/a \sim 1/4$  is the geometric probability of transit, and  $f_{\text{evap}} = t_{\text{evap}}/t_{\text{life}} \sim \{40, 400\} \text{ Myr} / 5 \text{ Gyr} \sim \{0.8, 8\}\%$  is the fraction of the planet’s lifetime spent in the catastrophic mass-loss stage. Inverting equation (34), we estimate that  $f_{\text{progenitor}} \sim \{1, 0.1\}\%$  of K stars harbor a close-in planet having less than the mass of Mercury.

For each KIC 1255b-like object there should be  $f_{\text{evap}}^{-1} = t_{\text{life}}/t_{\text{evap}} \sim \{130, 13\}$  planets with radii no larger than about Mercury’s ( $\leq 0.4 R_\oplus$ ), transiting K-type stars with sub-day periods. These planets have transit depths of  $(R/R_*)^2 \leq 10^{-5}$  — small but possibly detectable by *Kepler* if light curves are folded over enough periods (S. Rappaport 2012, personal communication) and if  $\dot{M} \sim \max \dot{M}$  so that the progenitor masses attain their maximum, Mercury-like values. If  $\dot{M}$  were actually  $\ll \max \dot{M}$ , the progenitor sizes would be less than that of Mercury. The smaller sizes would decrease their lifetimes  $t_{\text{evap}}$  and thus increase their expected number  $f_{\text{evap}}^{-1}$ , but would also render them undetectable even with *Kepler*.

#### 4.7 Iron Planets

In our model, we found the (maximum) present-day mass of KIC 1255b to be about 1/3 of its (maximum) mass at formation. If KIC 1255b began its life similar in composition to the rocky planets in the Solar System, evaporation may have stripped the planet of its silicate mantle, so that only its iron core remains: KIC 1255b could be an evaporating iron planet today.

We estimate mass loss rates of a pure iron planet using our isothermal model, including tidal gravity. We set the mean molecular weight of the gas to  $\mu_{\text{Fe}} \approx 56 m_H$  and use a bulk density for the planet of  $8.0$  g cm<sup>-3</sup>, appropriate for a pure iron planet of mass  $0.01 M_\oplus$  (Fortney et al. 2007). We fit laboratory measurements of the iron vapor pressure<sup>4</sup> at  $T = 2200$  K (Desai 1986) to equation (7), obtaining  $e^b = 7.8 \times 10^{11}$  dyne cm<sup>-2</sup> for a latent heat of sublimation  $L_{\text{sub}} = 6.3 \times 10^{10}$  erg g<sup>-1</sup> (Desai 1986) and  $m = \mu_{\text{Fe}}$ .

In Figure 10 we compare mass loss rates derived for the

<sup>4</sup> We have found measurements of the iron vapor pressure at  $T \sim 2000$  K to differ by a factor of two in the literature (see, e.g., Nuth et al. 2003).

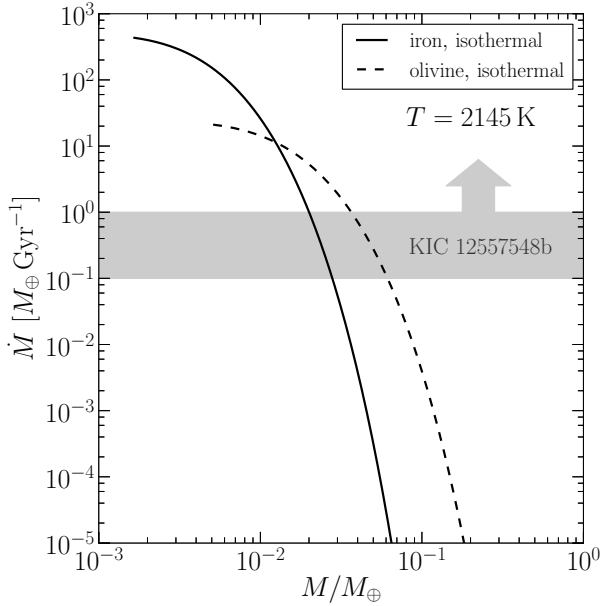


**Figure 10.** Mass loss rates  $\dot{M}$ , computed using the isothermal model at  $T = 2145 \text{ K}$ , for iron planets and olivine planets of varying  $M$ . In the low- $M$ , free-streaming limit, the higher vapor pressure of iron allows for a higher  $\dot{M}$  than for olivine. At larger  $M$ , mass loss rates are lower for iron planets than for olivine planets because of the higher molecular weight of iron. Our estimate for the maximum present-day mass of KIC 1255b varies by a factor of two between the iron and olivine scenarios.

isothermal model with  $T = 2145 \text{ K}$  for both an iron planet and a pure olivine planet. On the one hand, at this temperature, the vapor pressure for iron  $P_{\text{vapor, Fe}} = 1.8 \times 10^3 \text{ dyne cm}^{-2}$  is about 50 times higher than for olivine, which raises the mass loss rate by a similar factor in the free-streaming limit appropriate for low masses (see equation 28). On the other hand, at higher masses,  $\dot{M}$  for iron drops below that for olivine because the iron atmosphere, with its higher molecular weight, is harder to blow off. These two effects counteract each other so that an iron planet and a silicate planet both reach  $\dot{M}_{1255b} \sim 1 M_{\oplus} / \text{Gyr}$  at a similar  $M$ . Thus at least within the context of isothermal winds, our estimate for the present-day mass of KIC 1255b is insensitive to whether the evaporating surface of the planet is composed of iron or silicates. Figure 11 displays mass loss histories for an iron planet using our isothermal model at  $T = 2145 \text{ K}$ . Initial planet masses are up to a factor of two lower than those of our full model using silicates.

According to Figure 11, iron planets with  $M \gtrsim 0.05 M_{\oplus}$  survive for tens of Gyrs. Compare this result to its counterpart in Figure 9 (left panel), which shows that olivine planets with  $M \lesssim 0.1 M_{\oplus}$  evaporate within  $\sim 10 \text{ Gyr}$ . This comparison suggests that for planets with the right proportion of silicates in the mantle to iron in the core, mantles may be completely vaporized, leaving behind essentially non-evaporating iron cores. Such massive, quiescent iron cores might be detectable by *Kepler* via direct transits (see §4.6).

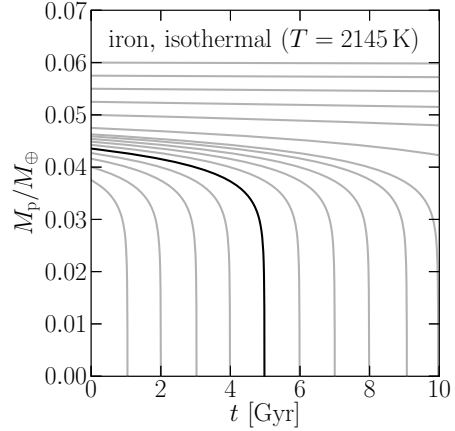


**Figure 11.** Mass-loss histories  $M(t)$  for an iron planet, obtained by time-integrating  $f_{\text{duty}} \cdot \max \dot{M}$  with  $f_{\text{duty}} = 0.5$  for an isothermal wind. An iron planet with a 5 Gyr lifetime will have an initial mass of  $\sim 0.044 M_{\oplus}$ . As was the case for olivine planets (see Figure 9), the catastrophic evaporation stage lasts only for  $\sim 100 \text{ Myr}$ . Iron planets (or planetary iron cores) with masses greater than  $0.05 M_{\oplus}$  survive for over 10 Gyr.

#### 4.8 Dust Condensation

Recall that we have not modelled the microphysics of dust formation, but treated the dust-to-gas ratio as a free function. Are the conditions of our flow actually favorable for the condensation of dust? Any gas whose partial pressure is greater than its vapor pressure (at that  $T$ ) might condense and form droplets (modulo the many complications discussed below). Condensation might proceed until all vapor in excess of saturation is in cloud particles. If the condensates have sedimentation velocities larger than updraft speeds they will rain out of the atmosphere; otherwise they remain aloft (see, e.g., Lewis 1969; Marley et al. 1999; Ackerman & Marley 2001; Helling et al. 2001).

In Figure 12, we compare gas pressures of our solutions (for  $\dot{M} = \max \dot{M}$ ) at  $M = 0.01, 0.03$ , and  $0.07 M_{\oplus}$  with the equilibrium vapor pressures of olivine and pyroxene. At the base of the flow, the gas pressure equals the saturation vapor pressure of olivine by construction. As gas expands and cools, its pressure generally remains above the saturation pressure of pyroxene, so conditions are favorable for the condensation of pyroxene grains. Unfortunately we have an embarrassment of riches: at  $T \lesssim 1700 \text{ K}$ , our gas pressures are many orders of magnitude higher than silicate vapor pressures, and the concern is that gas condensation will lower pressures precipitously to the point where winds shut down. This fate could be avoided if grains take too long to condense out of the outflowing and rapidly rarefying gas — i.e., the finite timescale of grain condensation might permit gas to remain supersaturated. Furthermore, even before bulk condensation can begin, seed particles must first nucleate from the gas phase. These issues call for a time-dependent analysis of grain formation, perhaps along the lines made for brown dwarf and exoplanet atmospheres (Helling et al. 2001, 2008a,b; Helling & Rietmeijer 2009). Accounting for the extra heating from small grains with sizes  $\ll 1 \mu\text{m}$  as they first condense out of the wind (§4.2) would keep the gas closer to isothermal and help to prevent catastrophic condensation.

Of course, by the wind leaves the sonic point and is diverted into the trailing comet-like tail, it must be full of grains to explain

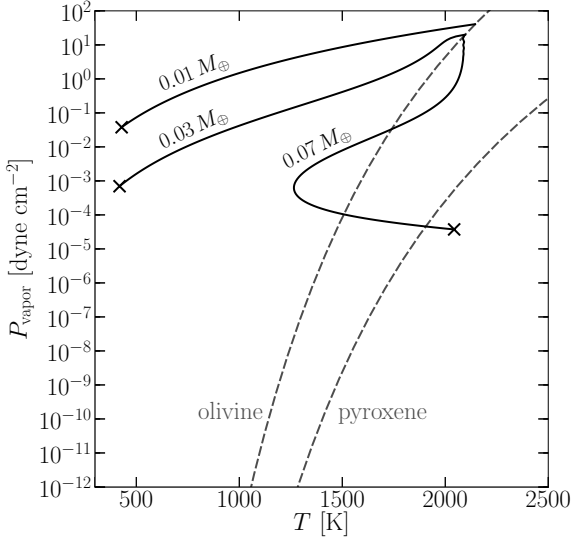


**Figure 12.** Trajectories of the wind in pressure-temperature space, computed using the full model for  $M = 0.01, 0.03$ , and  $0.07 M_{\oplus}$ . Gas pressures generally remain above the equilibrium vapor pressures of pyroxene, permitting the condensation of pyroxene grains.

the observed occultations of KIC 1255b. In this paper, we have not modeled the dusty tail at all. Future work should address the dynamics of the tail and compute its extinction profile, with the aim of reproducing the observed transit lightcurves.

## 5 CONCLUSIONS

Our work supports the hypothesis that the observed occultations of the K-star KIC 12557548 originate from a dusty wind emitted by an evaporating planetary companion (“KIC 1255b”). We reach the following conclusions.

### (i) Maximum present-day mass

Our estimates for the maximum present-day mass of KIC 1255b range from  $\max M \approx 0.02 M_{\oplus}$  (roughly twice the mass of the Moon) to  $\max M \approx 0.07 M_{\oplus}$  (slightly larger than the mass of Mercury), depending on how strongly the wind is heated by dust and can remain isothermal (Figure 8). For these maximum masses, calculated mass loss rates peak at  $\max \dot{M} \sim 0.1 M_{\oplus}/\text{Gyr}$ , which is just large enough to produce the observed transit depths of order 1%. Smaller planets with weaker gravities yield larger mass loss rates and are also compatible with the observations.

### (ii) Maximum formation mass

For an assumed planet age of  $\sim 5$  Gyr, the maximum mass of KIC 1255b at formation ranges from  $0.06 M_{\oplus}$  to  $0.1 M_{\oplus}$ , again depending on the energetics of the wind (Figure 9).

### (iii) Mass threshold for catastrophic evaporation

A pure rock planet of mass  $\gtrsim 0.1 M_{\oplus}$  and surface temperature  $\leq 2200$  K will survive with negligible mass loss for tens of Gyrs.

### (iv) Time variability

The observed occultations of KIC 12557548 vary by up to an order of magnitude in depth without any apparent correlation between orbits. The implied order-of-magnitude variations in  $\dot{M}$  can be explained in principle by the exponential sensitivity of  $\dot{M}$  to condi-

tions at the planet surface. The dynamical “refresh” timescale of the wind  $t_{\text{dyn}} \sim 14$  h is similar to the orbital period  $P_{\text{orb}} = 15.7$  h. This supports our dusty wind model because were  $t_{\text{dyn}} \gg P_{\text{orb}}$  or  $t_{\text{dyn}} \ll P_{\text{orb}}$ , then eclipse depths would correlate from orbit to orbit, in violation of the observations.

### (v) Progenitors and occurrence rates

KIC 1255b’s current catastrophic mass loss phase may represent only the final few percent of the planet’s life. As such, for every KIC 1255b-like object, there could be anywhere from 10 to 100 larger planets in earlier stages of mass loss. These close-in, relatively quiescent progenitors may be detectable by *Kepler* through conventional “hard-sphere” transits if they are as large as Mercury. We cannot, however, rule out the possibility that the progenitors are lunar-sized or even smaller. If KIC 1255b remains the only catastrophically evaporating planet in the *Kepler* database, then the occurrence rate of close-in progenitors orbiting K-stars with sub-day periods is  $> 0.1\%$ , with larger occurrence rates for progenitors increasingly smaller than Mercury.

### (vi) Iron planet

KIC 1255b may have lost  $\sim 70\%$  of its formation mass to its thermal wind. It seems possible that today only the iron core of KIC 1255b remains and is evaporating. Transmission spectra of the occulting dust cloud might reveal whether the planet’s surface is composed primarily of iron or silicates.

### (vii) Future modelling and observations

Keeping the wind hot as it lifts off the planet surface significantly enhances mass loss rates. In our model we have included heating of the gas by micron-sized grains embedded in the flow. But these grains can also shadow the surface from starlight and reduce  $\dot{M}$  if they are too abundant. Additional heating may be provided by super-blackbody grains with sizes  $\ll 1 \mu\text{m}$  which do not significantly attenuate starlight. Future models should incorporate such tiny condensates — and treat the dusty comet-like tail that our paper has completely ignored. More information about grain size distributions and compositions might be revealed by *Hubble* observations of KIC 12557548 scheduled for early 2013.

## 6 ACKNOWLEDGMENTS

We thank Saul Rappaport for alerting us to the feasibility of detecting Mercury-sized progenitors of KIC 1255b using *Kepler*, and Andrew Howard and Geoff Marcy for sharing their Keck observations of KIC 12557548. We are also grateful to Andrew Ackerman, Tom Barclay, Bill Borucki, Raymond Jeanloz, Hiroshi Kimura, Edwin Kite, Michael Manga, Mark Marley, and Subu Mohanty for useful and encouraging conversations; to Paul Kalas for pointing us to work on beta Pictoris that presaged the story of KIC 1255b; and to an anonymous referee for a helpful report that motivated us to review the various modeling uncertainties and introduced us to the cloud formation literature. D.P.-B. acknowledges the support of a UC MEXUS-CONACyT Fellowship. E.C. acknowledges *Hubble Space Telescope* grant HST-AR-12823.01-A.

## REFERENCES

- Ackerman, A. S. & Marley, M. S. 2001, *ApJ*, 556, 872
- Anderson, B. J., Acuña, M. H., Korth, H., et al. 2008, *Science*, 321, 82

- Batalha, N. M., Borucki, W. J., Koch, D. G., et al. 2010, *ApJ Letters*, 713, L109
- Ben-Jaffel, L. 2007, *ApJ Letters*, 671, L61
- Ben-Jaffel, L. 2008, *ApJ*, 688, 1352
- Bida, T. A., Killen, R. M., & Morgan, T. H. 2000, *Nature*, 404, 159
- Brogi, M., Keller, C. U., de Juan Ovelar, M., et al. 2012, *A&A*, 545, L5
- Catling, D. C. & Zahnle, K. J. 2009, *Scientific American*, 300, 050000
- Chiang, E. & Laughlin, G. 2013, *MNRAS*
- Desai, P. D. 1986, *Journal of Physical and Chemical Reference Data*, 15, 967
- Ekenbäck, A., Holmström, M., Wurz, P., et al. 2010, *ApJ*, 709, 670
- Fortney, J. J., Marley, M. S., & Barnes, J. W. 2007, *ApJ*, 659, 1661
- Fossati, L., Haswell, C. A., Froning, C. S., et al. 2010, *ApJ Letters*, 714, L222
- García Muñoz, A. 2007, *Planetary & Space Science*, 55, 1426
- Geissler, P. E. 2003, *Annual Review of Earth and Planetary Sciences*, 31, 175
- Hansen, B. M. S. & Murray, N. 2012, *ApJ*, 751, 158
- Hashimoto, A. 1990, *Nature*, 347, 53
- Helling, C., Ackerman, A., Allard, F., et al. 2008a, *MNRAS*, 391, 1854
- Helling, C., Oevermann, M., Lüttke, M. J. H., Klein, R., & Sedlmayr, E. 2001, *A&A*, 376, 194
- Helling, C. & Rietmeijer, F. J. M. 2009, *International Journal of Astrobiology*, 8, 3
- Helling, C., Woitke, P., & Thi, W.-F. 2008b, *A&A*, 485, 547
- Holmström, M., Ekenbäck, A., Selsis, F., et al. 2008, *Nature*, 451, 970
- Jakosky, B. M. & Phillips, R. J. 2001, *Nature*, 412, 237
- Kasting, J. F. & Pollack, J. B. 1983, *Icarus*, 53, 479
- Killen, R. M., Sarantos, M., Potter, A. E., & Reiff, P. 2004, *Icarus*, 171, 1
- Kim, R.-S., Gopalswamy, N., Moon, Y.-J., Cho, K.-S., & Yashiro, S. 2012, *ApJ*, 746, 118
- Kimura, H., Mann, I., Biesecker, D. A., & Jessberger, E. K. 2002, *Icarus*, 159, 529
- Kohl, J. L., Noci, G., Antonucci, E., et al. 1998, *ApJ Letters*, 501, L127
- Lai, D., Helling, C., & van den Heuvel, E. P. J. 2010, *ApJ*, 721, 923
- Lamers, H. J. G. L. M. & Cassinelli, J. P. 1999, *Introduction to Stellar Winds*
- Lamers, H. J. G. L. M., Lecavelier Des Etangs, A., & Vidal-Madjar, A. 1997, *A&A*, 328, 321
- Lammer, H. & Bauer, S. J. 1997, *Planetary & Space Science*, 45, 73
- Lange, N. A. & Forker, G. M. 1967, *Handbook of Chemistry*
- Lecavelier des Etangs, A., Bourrier, V., Wheatley, P. J., et al. 2012, *A&A*, 543, L4
- Lecavelier Des Etangs, A., Ehrenreich, D., Vidal-Madjar, A., et al. 2010, *A&A*, 514, A72
- Lecavelier Des Etangs, A., Vidal-Madjar, A., Burki, G., et al. 1997, *A&A*, 328, 311
- Lewis, J. S. 1969, *Icarus*, 10, 365
- Linsky, J. L., Yang, H., France, K., et al. 2010, *ApJ*, 717, 1291
- Llama, J., Wood, K., Jardine, M., et al. 2011, *MNRAS*, 416, L41
- Lopez, E. D., Fortney, J. J., & Miller, N. 2012, *ApJ*, 761, 59
- Marley, M. S., Gelino, C., Stephens, D., Lunine, J. I., & Freedman, R. 1999, *ApJ*, 513, 879
- McComas, D. J., Elliott, H. A., Schwadron, N. A., et al. 2003, *Geophys. Res. Lett.*, 30, 1517
- Melosh, H. J. & Vickery, A. M. 1989, *Nature*, 338, 487
- Mura, A., Wurz, P., Schneider, J., et al. 2011, *Icarus*, 211, 1
- Murray, C. D. & Dermott, S. F. 1999, *Solar system dynamics*
- Murray-Clay, R. A., Chiang, E. I., & Murray, N. 2009, *ApJ*, 693, 23
- Nagahara, H., Mysen, B. O., & Kushiro, I. 1994, *Geochimica et Cosmochimica Acta*, 58, 1951
- Ness, N. F., Behannon, K. W., Lepping, R. P., Whang, Y. C., & Schatten, K. H. 1974, *Science*, 185, 151
- Nuth, III, J. A., Ferguson, F. T., Johnson, N., & Martinez, D. 2003, in *Lunar and Planetary Inst. Technical Report*, Vol. 34, Lunar and Planetary Institute Science Conference Abstracts, ed. S. Mackwell & E. Stansbery, 1598
- Potter, A. E. & Morgan, T. H. 1990, *Science*, 248, 835
- Potter, A. E. & Morgan, T. H. 1997, *Planetary & Space Science*, 45, 95
- Press, W. H., Teukolsky, S. A., Vetterling, W. T., & Flannery, B. P. 1992, *Numerical recipes in C. The art of scientific computing*
- Quémerais, E., Lallement, R., Koutroumpa, D., & Lamy, P. 2007, *ApJ*, 667, 1229
- Rappaport, S., Levine, A., Chiang, E., et al. 2012, *ApJ*, 752, 1
- Schaefer, L. & Fegley, B. 2009, *ApJ Letters*, 703, L113
- Sheeley, Jr., N. R., Wang, Y.-M., Hawley, S. H., et al. 1997, *ApJ*, 484, 472
- Swift, J. J., Johnson, J. A., Morton, T. D., et al. 2013, *ApJ*, 764, 105
- Tachibana, S., Tsuchiyama, A., & Nagahara, H. 2002, *Geochimica et Cosmochimica Acta*, 66, 713
- Tian, F., Toon, O. B., Pavlov, A. A., & De Sterck, H. 2005, *ApJ*, 621, 1049
- Tremblin, P. & Chiang, E. 2013, *MNRAS*, 428, 2565
- Vidal-Madjar, A., Désert, J.-M., Lecavelier des Etangs, A., et al. 2004, *ApJ Letters*, 604, L69
- Vidal-Madjar, A., Lecavelier des Etangs, A., Désert, J.-M., et al. 2003, *Nature*, 422, 143
- Vidal-Madjar, A., Lecavelier des Etangs, A., Désert, J.-M., et al. 2008, *ApJ Letters*, 676, L57
- Vidotto, A. A., Jardine, M., & Helling, C. 2010, *ApJ Letters*, 722, L168
- Vidotto, A. A., Jardine, M., & Helling, C. 2011a, *MNRAS*, 411, L46
- Vidotto, A. A., Jardine, M., & Helling, C. 2011b, *MNRAS*, 414, 1573
- Watson, A. J., Donahue, T. M., & Walker, J. C. G. 1981, *Icarus*, 48, 150
- Yelle, R. V. 2004, *Icarus*, 170, 167
- Yelle, R. V. 2006, *Icarus*, 183, 508
- Youdin, A. N. & Shu, F. H. 2002, *ApJ*, 580, 494
- Zahnle, K., Pollack, J. B., Grinspoon, D., & Dones, L. 1992, *Icarus*, 95, 1
- Zahnle, K. J. & Kasting, J. F. 1986, *Icarus*, 68, 462